Coherence-Based Prediction of Multi-Temporal InSAR Measurement Availability for Infrastructure Monitoring

Malinowska, Dominika; Milillo, Pietro; Briggs, Kevin; Reale, Cormac; Giardina, Giorgia

DOI
10.1109/JSTARS.2024.3449688

Publication date
2024

Document Version
Final published version

Published in
IEEE Journal of Selected Topics in Applied Earth Observations and Remote Sensing

Coherence-Based Prediction of Multi-Temporal InSAR Measurement Availability for Infrastructure Monitoring

Dominika Malinowska, Pietro Milillo, *Senior Member, IEEE*, Kevin Briggs, Cormac Reale, and Giorgia Giardina

***Abstract*—Predicting the availability of measurement points provided by Multi-Temporal Interferometric Synthetic Aperture Radar (MT-InSAR) poses a challenge due to a nonuniform distribution of Persistent Scatterers (PSs). This article introduces a novel method to estimate the availability of MT-InSAR results on buildings and infrastructure networks, eliminating the need for labor-intensive and time-consuming analyses of the entire SAR data stack. The method is based on an analysis of the interferometric coherence decay characteristics and data regarding buildings and transport infrastructure location as inputs to a convolutional neural network. Specifically, a U-Net architecture model was implemented and trained to predict the PS density of Sentinel-1 data. The methodology was applied to a regional-scale analysis of the Dutch infrastructure, resulting in a low 1.06±0.10 mean absolute error in the pixel-based PS count estimation on the test data split, with over 80% of predictions within ±1 from the actual value. The model achieved high accuracy when applied to a previously unseen dataset, demonstrating strong generalization performance. The proposed workflow, with its notable ability to accurately predict areas lacking measurement points, offers stakeholders a tool to assess the feasibility of applying MT-InSAR for specific structures. Thereby, it enhances infrastructure reliability by addressing a critical need in decision-making processes and improving the applicability of MT-InSAR for structural health monitoring of infrastructure assets.**

Received 8 February 2024; revised 25 June 2024 and 5 August 2024; accepted 17 August 2024. Date of publication 26 August 2024; date of current version 20 September 2024. This work was supported in part by the Vidi project InStruct, project number 18912, financed by the Dutch Research Council (NWO), in part by the University of Houston under a contract with the Commercial Smallsat Data Scientific Analysis Program of NASA under Grant NNH22ZDA001N-CSDSA, and in part by the Decadal Survey Incubation Program: Science and Technology under Grant NNH21ZDA001N-DSI. The work of Kevin Briggs was supported by the Royal Academy of Engineering and HS2 Ltd. through the Senior Research Fellowship scheme under Grant RCSRF1920_10_65. *(Corresponding author: Dominika Malinowska.)*

Dominika Malinowska is with the Department of Geoscience and Engineering, Delft University of Technology, 2628 CD Delft, The Netherlands, and also with the Department of Architecture and Civil Engineering, University of Bath, BA2 7AY Bath, U.K. (e-mail: d.u.malinowska@tudelft.nl).

Pietro Milillo is with the Cullen College of Engineering, Department of Civil and Environmental Engineering, University of Houston, Houston, TX 77004 USA, and also with the Microwaves and Radar Institute, German Aerospace Center, 82234 Weßling, Germany.

Kevin Briggs is with the Faculty of Engineering and Physical Sciences, University of Southampton, SO17 1BJ Southampton, U.K.

Cormac Reale is with the Department of Architecture and Civil Engineering, University of Bath, BA2 7AY Bath, U.K.

Giorgia Giardina is with the Department of Geoscience and Engineering, Delft University of Technology, 2628 CD Delft, The Netherlands.

Digital Object Identifier 10.1109/JSTARS.2024.3449688

***Index Terms*—Neural networks, rail transportation, remote sensing, road transportation.**

I. Introduction

TRANSPORT infrastructure plays a crucial role in global socioeconomic development [1]. Regular inspections of roads and railways are an essential part of asset management and are imperative to ensure reliable transportation networks [2]. Stakeholders are actively exploring new monitoring tools that can aid and inform decision-making processes, enhancing infrastructure asset management strategies [3]. Infrastructure monitoring typically relies on in-situ visual inspection, a labor-intensive process that provides subjective reports of varying quality, e.g., differences in assigned condition scores [4], [5]. Wired and wireless sensors can be installed on some structures to mitigate the subjectivity of surveys and increase measurement frequency. However, operating and installing these sensors can be expensive [6]. Moreover, inspecting the condition of transportation infrastructure remains challenging even when using a network of wireless sensors, due to the geographical extent and linear nature of transport networks [7].

Remote sensing techniques have emerged as a promising solution to address the economic and practical challenges associated with conventional inspections and sensor installations. These techniques encompass a range of technologies, including cameras, mobile devices, drones, robots, and satellites [8], [9]. Satellite-based methods can cover extensive areas and monitor multiple structures simultaneously, which is particularly advantageous when monitoring linear infrastructure [10].

A widely employed satellite-based technology for infrastructure monitoring is Synthetic Aperture Radar (SAR), an active sensor emitting electromagnetic waves and recording backscattered signals [11]. SAR imagery contains data on amplitude and phase, where amplitude represents signal strength and phase enables distance measurements. Interferometric SAR (InSAR) techniques leverage phase differences between two SAR acquisitions to generate interferograms, enabling the detection of temporal changes and quantification of target movements [12], [13]. An interferogram is created by pixelwise cross-multiplication of one SAR image with a complex conjugate of a second one to reveal phase differences between the images. Since its first application to earthquake mapping [14], InSAR has become

a standard approach for Earth's surface deformation monitoring [15]. However, InSAR faces challenges related to variations in terrain reflective properties [16] and radar signal delays due to water vapor in the atmosphere [17], negatively impacting its accuracy and applicability. Multi-temporal InSAR (MT-InSAR) analysis, which processes a stack of radar images, overcomes the limitations of traditional InSAR techniques by processing only selected pixels. MT-InSAR exploits phase information from multiple interferograms to measure the temporal displacement of point-like targets called Persistent Scatterers (PSs) defined by specific backscatter characteristics [18], [19].

MT-InSAR has gathered increased attention as a prospective solution for infrastructure monitoring, offering a wide-scale and cost-effective approach to Structural Health Monitoring (SHM) [20], [21], [22]. However, one of the key challenges impeding the widespread adoption of MT-InSAR as a complementary method to other SHM techniques relates to the predictability of its outcomes. Although MT-InSAR can achieve millimeter-level accuracy in monitoring certain structures [23], [24], it may not be applicable to all components of a transportation network, as this technique provides observations for specific pixels, potentially leaving some structures without any measurement points [25].

This article presents a new method for the rapid assessment of the applicability of remote sensing techniques for monitoring of buildings and transport infrastructure. This addresses the need for a preliminary evaluation of the availability of remote sensing results, eliminating the requirement of time-consuming data analysis of the entire data stack. To achieve this aim, we first analyzed attributes of MT-InSAR, particularly focusing on interferometric coherence, and identified parameters that showed a good correlation with PS availability. We then generated an infrastructure map with values showing the likelihood of PS detection depending on the structure type. Next, through the utilization of machine learning (ML) techniques, we developed a model of the correlation between coherence decay parameters, data about infrastructure presence, and PS availability. The methodology was applied to structures in urban environments and transportation networks that will be referred to as infrastructure in the remainder of the article. The article's key contributions are summarized as follows.

1) A workflow was proposed for predicting the availability of MT-InSAR outcomes, providing stakeholders with valuable insights for informed decision-making regarding the feasibility of a structure for spaceborne monitoring.
2) The developed methodology demonstrated good capabilities in predicting PS availability from the Sentinel-1 dataset and proved its generalization ability by performing well on unseen data.

The rest of this article is organized as follows. Section II provides an overview of the reasons behind the nonuniform PS availability and a literature summary of previous approaches proposed for PS density estimation. Section III describes the specific case study, the data sources utilized in the analysis, and the methodology employed. Section IV presents the results of the proposed model. In Section V, these results are critically discussed. Finally, Section VI concludes this article.

II. Background

Several factors affect the ability to detect PSs on specific structures through MT-InSAR. First, the characteristics of a SAR sensor have a prominent impact. Longer radar wavelengths yield coarser resolution and, consequently, sparser PS detection [26], [27]. Furthermore, SAR satellites typically follow sun-synchronous near-polar orbits. PSs on transportation networks are usually generated by reflections from elements along the structure length, such as road edges, bridge sides, or traffic barriers, while road surface tends to reflect most of the energy away from the satellite. Therefore, structures aligned in North–South directions can potentially provide fewer PSs [20]. Geometrical distortions inherent to SAR data due to its side-looking nature further complicate the issue [17], [28]. These are the most pronounced in mountainous or densely built-up regions with tall structures, rendering some pixels unsuitable for PS detection [20]. Attempts have been made to model these distortions using topography maps and radar geometry to assess PS detectability [29], [30], [31], [32], [33], [34], [35], [36]. However, these models have primarily focused on landslide applications and are less applicable to urban areas, which are of greater significance in infrastructure monitoring. While a SAR simulator has been proposed for creating 3-D models of structures to predict shadow zones and geometric effects [37], it remains a labor-intensive process, necessitating in-depth knowledge of the target geometry.

Second, the properties of the target structure play a pivotal role in determining whether a pixel can function as a PS. Effective PS detection relies on radar waves being reflected back to the satellite with sufficient strength and in the appropriate direction, and target backscatter characteristics depend on its size, shape, roughness, and dielectric constant [38], [39]. Urban areas typically exhibit favorable properties for strong backscatter and PS generation [40], [41]. Thus, assuming that any pixel intersecting with a man-made object can be a potential PS target, a building database and topographic map can be used for a preliminary assessment of PS detection probability [26]. In this approach, measuring the distance between potential PS points and assessing PS distribution is also crucial, as points forming clusters are deemed to be more suitable for PS analysis. However, this method tends to overestimate the PS density when compared to actual results, illustrating the challenge of determining suitable radar targets among all man-made objects. Nevertheless, correlations between land cover type and PS density can provide rough estimates of PS distribution for specific regions. Authors of such methods typically derive empirical PS density values for various land cover types and sensors, proposing their independent use [26] or in combination with geometric distortion modeling [29], [30], [31], [32], [33], [34], [35], [36]. As these techniques were initially designed for landslide observation, they present challenges when applied to infrastructure monitoring. While those correlations can be extrapolated to new study areas, PS density is typically assumed to be uniform within a land cover class, reducing accuracy. As land cover maps often possess coarse resolution, they might not adequately account for infrastructure elements in rural areas that could be otherwise

classified as urban regions, further reducing the accuracy of prediction.

Third, PSs are only identified in pixels with stable reflective properties over time. Changes such as alterations in vegetation, temporary snow cover, structural maintenance, damage, or heavy traffic can disrupt signal backscattering and render a pixel unsuitable as a measurement point [25]. Empirical correlations between PS density and Normalized Difference Vegetation Index (NDVI) have been proposed [30]. However, their effectiveness in highly vegetated areas is limited by the availability of high-resolution NDVI data, making them most suitable for sparsely vegetated regions. Another approach involves the use of an amplitude dispersion index to exclude pixels significantly affected by changes in reflective properties over time [29]. While this method effectively filters out pixels of the lowest quality, it does not account for situations where amplitude remains stable, but other factors render a pixel unusable.

Given the multitude of factors affecting the visibility of structures in MT-InSAR results, assessing the suitability of infrastructure assets for spaceborne monitoring remains a complex task, even for experienced individuals. Although several techniques have been proposed for predicting PS density prior to MT-InSAR processing, they are predominantly designed for landslide monitoring and may yield inaccurate results in the context of infrastructure, particularly for structures such as bridges [42]. Methods for estimating if a deformation of a linear infrastructure is measurable when applying MT-InSAR to data from a particular set of satellites exist, but they operate under the assumption that PSs are available [43].

Attempts have been made to train ML models to predict not only PS density but also precise displacement measurements for road infrastructure [44], [45]. However, obtaining comprehensive datasets comprising hydrological, geomorphometric, geomorphological, and social attributes of a terrain, alongside existing PS results required as input to such a model, can be challenging for many transportation networks. Consequently, effective methods are still needed to assess the suitability of MT-InSAR for infrastructure monitoring that does not necessitate extensive data analysis across an entire data stack.

Previous approaches to predicting PS density, as described above, primarily involved directly modeling factors influencing PS availability. However, a relationship has been observed between PS density and certain attributes of MT-InSAR, namely, the coherence values within a differential interferogram [19]. Interferometric coherence quantifies the change between the two images in an interferogram by measuring the correlation between phase values [12]. This correlation indicates the reliability and readability of the phase, and it is used to assess the quality of the interferogram. The coherence is spatially averaged over a few pixels, which minimizes biases inherent to interferometry, but in turn, makes it impossible to easily employ this parameter for the identification of PSs as these are smaller than one resolution cell [18], [46]. Nonetheless, permanent scatters, by definition, maintain high coherence over time [18]. Therefore, regions with high interferometric coherence should be relatively densely populated with PSs. Still, a PS can be formed in an area characterized by a low interferometric coherence if the coherence is stable over the study period.

A long-term coherence parameter that measures the temporal decorrelation over the spatially averaged SAR resolution cells has been proposed to quantify interferometric coherence changes over time [47], [48], and a global seasonal long-term coherence dataset has been previously published [49]. The long-term coherence accounts for the lack of complete decorrelation of some pixels and is significantly higher for artificial scatterers when compared to vegetated areas, owing to the former's ability to offer more stable reflections [47]. The fact that artificial scatterers remain coherent over time is what makes them better PS candidates, so a higher PS density should be expected for pixels with high long-term coherence.

The correlation between long-term coherence and PS density is not trivial, primarily because of the spatial averaging involved in coherence calculation and its association with the physical properties of a target. As far as the authors are aware, this correlation has not been investigated to date. While linear regression could potentially model such a correlation, the spatial complexities render it an unsuitable choice for this case. However, various ML techniques have been developed to model similarly complex relationships, including cases where the correlation entails a spatial component. Specifically, Fully Convolutional Neural Networks (FCNNs) were introduced to address pixel-dense problems in computer vision [50], [51]. The U-Net architecture [52], an extension to FCNNs, has been adapted for semantic segmentation of remote sensing data, including land cover classification [53], sea-land segmentation [54], cloud detection [55], road extraction [56], [57], building extraction [58], and building damage classification [59]. However, U-Net can also be applied to pixelwise regression tasks where the ML model is trained to predict continuous variables. In the field of remote sensing, this method has been used for pansharpening [60], estimation of sea ice concentration [61], or bathymetry derivation [62], to name a few.

III. Materials and Methods

A methodology was developed in this study to estimate the availability of MT-InSAR measurements on buildings and transportation networks. The method takes information on coherence decay characteristics and data regarding infrastructure location as inputs to a convolutional neural network designed and trained to predict PS density. The coherence decay was investigated through the seasonal long-term coherence dataset [49]. This dataset provides information globally on how interferometric coherence changes in a given season with the increased time between image acquisitions. Long-term seasonal coherence variations were examined in combination with NDVI. Seasonal NDVI statistics, specifically mean and standard deviation, were analyzed to explain the changes in the long-term coherence. Those observations were used to select the season best suited as input for the proposed technique. A geospatial dataset of buildings and linear infrastructure was processed to generate

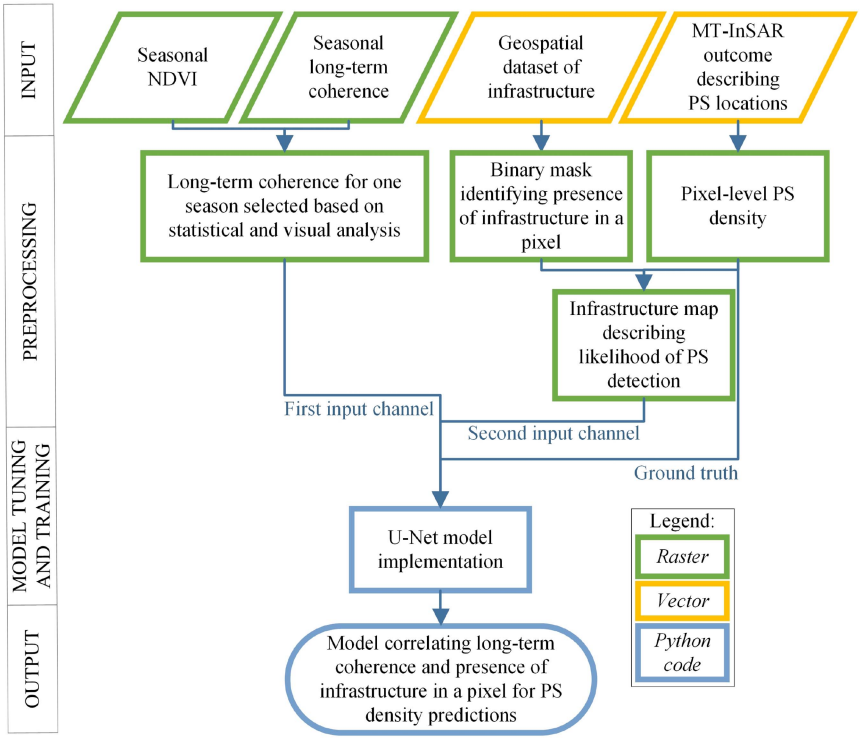

Fig. 1. Flowchart illustrating the step-by-step methodology.

pixel-level information on infrastructure presence. Existing MT-InSAR findings were examined to gather information on the PSs densities. By integrating information about infrastructure location and PS density, an infrastructure map was generated where values corresponded to the likelihood of PS detection for selected infrastructure typologies. A U-Net model designed for a pixelwise regression task was implemented. This model used the seasonal long-term coherence and the infrastructure map as inputs and the density map generated from existing MT-InSAR results as ground truth to assess the model's performance through a comparison with the pixel-based PS count predictions. Fig. 1 outlines the steps followed to model the correlation between long-term coherence, infrastructure presence, and density of PSs.

A. Case Study

Data for the ML model's training, validation, and testing were acquired over the Netherlands. The Area of Interest (AoI) spanned between 3° and 8° East and 50° and 54° North to ensure comprehensive coverage (see Fig. 2), taking into consideration that some of the input data were in tiled format.

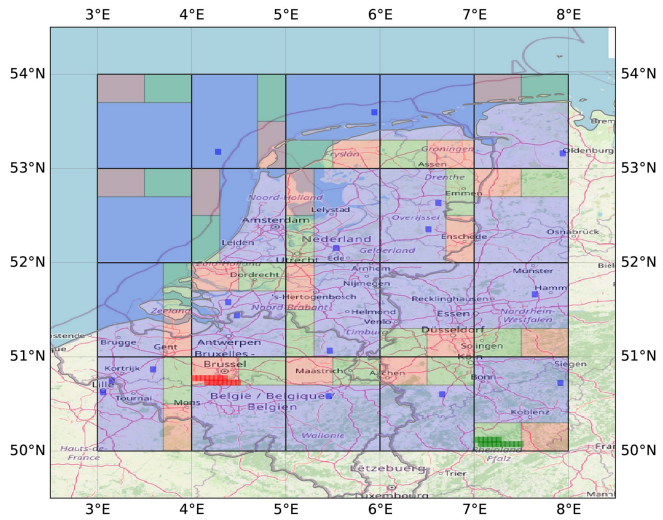

Fig. 2. Regional-scale dataset over the Netherlands, incorporating coherence decay, infrastructure location, and MT-InSAR outcomes. The coherence dataset comprises 20 tiles (black outlined squares), while other data sources are represented by a single tile covering the entire AoI. Each tile underwent random division into training (blue), validation (red), and test (green) datasets.

B. Data Sources

1) Interferometric Coherence: A global seasonal interferometric coherence and backscatter dataset by Kellndorfer et al. [49] was used as one of the model inputs. This dataset results from the analysis of a stack of Sentinel-1 images. Covering most of the world, the dataset is subdivided seasonally (winter: December–February 2019/20, spring: March–May 2020, summer: June–August 2020, and fall: September–November 2020). Acquisitions from the descending flight direction of Sentinel-1 are used for most of the world, including the AoI considered in this article. The interferometric coherence is calculated for each seasonal substack with various repeat times, i.e., the number of

days between acquisitions. Moreover, coherence decay model parameters are provided. The data are published with three arcsec pixel spacing resolution (≈90 m at the equator). The dataset is provided in VV and HH polarization. We chose to use the former as this is the polarization commonly used for MT-InSAR applications.

A few models of temporal decorrelation have been proposed in the literature [47], [48]. The data provided in [49] utilize the following model adopted from [47]:

$$\rho_{\text{temp}}(t) = (1 - \rho_{\text{LT}})e^{-\frac{t}{\tau}} + \rho_{\text{LT}} \tag{1}$$

where the temporal decorrelation $\rho_{\text{temp}}(t)$ is considered to be related to the time between acquisitions t, the target decorrelation factor τ indicates the rate of the exponential decrease in days, and the long-term coherence ρ_{LT} is accounting for the fact that some pixels never completely decorrelate. In [49], multiple seasonal stacks of SAR images were created with variable repeat intervals, and the pixel-level coherence was calculated for each of them. Then, given the known coherence and time interval, an exponential curve was fitted to estimate the parameters τ and ρ_{LT} for each pixel. In this study, the seasonal long-term coherence was analyzed and used as input to the ML model due to its correlation with the PS presence, as explained in Section II.

2) NDVI: The NDVI, a metric derived from optical remote sensing data and used for vegetation quantity estimation [63], [64], [65], was generated using Sentinel-2 images through Google Earth Engine (GEE). The NDVI is calculated by normalizing the difference between near-infrared and red wavelengths, both having a 10 m resolution. All Sentinel-2 images with less than 50% cloud coverage from the seasonal time frames matching the global coherence study were considered in the processing. A mask was used to remove the remaining clouds and shadows. Then, the mean across all available images for each season was calculated. The four seasonal NDVI rasters were resampled to match the resolution of other rasters used in the study. It should be noted that for some pixels, all images within the seasonal time frame were covered by a cloud or shadow, so obtaining the NDVI value for that season was impossible.

3) Infrastructure Networks: Open Street Map (OSM) was employed to identify pixels that cover infrastructure. While the quality of the OSM database relies on a community of volunteers, it exhibits a high level of accuracy [66]. As of January 2016, the road network was estimated to be over 80% complete [67]. However, there is significant global variation, with over 40% of countries having more than 95% completion, while others, such as China, Egypt, and Pakistan, have less than 30% of streets reported. Some other large countries, such as Russia and India also have less than half of their road networks mapped. A more recent analysis indicates that building completeness is high in Europe, Central Asia, and North America but remains low in regions such as South Asia and parts of Africa [68]. Nevertheless, the database is rapidly expanding, especially in developing countries, with completeness increasing annually [67], [68]. As an example, the covered length of the Iranian road network increased 110 times from 2008 to 2016 [69]. In addition, a study on Chinese roads found that while overall completeness is low, over 80% of roads with high traffic conditions are reported in the OSM [70]. This suggests that important major roads are likely mapped and is confirmed by the observation that missing roads are often private residential roads or single-line roads and, thus, less significant for this study. Therefore, the OSM database remains the best available source of infrastructure data for studies on the national or even global level.

We extracted entries within the AoI for buildings, railways, and road networks (motorways, trunks, primary and secondary highways, specifically). The railways and road networks in the OSM are provided as linear features on a vector layer representing the middle line of a road, while buildings are shown as polygons. Each of those datasets was rasterized, ensuring resolution consistent with other inputs so that all pixels touched by either a line or a polygon were assigned a value of 1 while the rest had a value of 0. The AoI encompassed 32 338 km of railways, 13 762 km of motorways, 4782 km of trunk, 18 494 km of primary roads, and 32 712 km of secondary roads. Buildings covering a planar area of 3535 km^2 were also considered.

4) PSs Location: For information about PSs location, data from the European Ground Motion Service (EGMS) derived from Sentinel-1 images acquired between 2018 and 2022 were used [42], [71]. EGMS is an initiative providing European-wide Advanced Differential InSAR (A-DInSAR) results.[1] The EGMS deformation maps are generated separately for ascending and descending orbits. For this article, we employed data from the descending flight direction. All frames covering the AoI were downloaded and processed to obtain pixel-level PS density. If frames overlapped, the higher values were retained. To focus on PSs, distributed scatterers (DS) that were introduced to the EGMS data as a complementary source of information where data coverage was not up to the project requirements were removed [72]. This was achieved by setting a filter on the "effective area" parameter that is zero for PSs and using the resulting PS map for pixel-level PS density calculation.

C. Methodology

1) Preprocessing of Input Data: As the first step in the workflow, we preprocessed the data to ensure its suitability as one of the two input channels for the ML model. The seasonal long-term coherence datasets were compared through a visual and statistical analysis to identify the season yielding optimal results. The objective was to determine the season that allowed the model to distinguish infrastructure from other elements most effectively.

Information about PSs location from EGMS data was processed to generate pixel-based PS density maps. First, a grid with three arcsec (≈90 m at the equator) resolutions was generated, and the number of PSs in each square was counted. Then, the grid was rasterized so that the value of each pixel represented the PS density. The generated PS density map served as the ground truth for model training.

[1]In this context, A-DInSAR is used as a collective word referring to all InSAR techniques analyzing big stacks of data covering spatially wide areas. It encompasses methods that provide PS, DS, and hybrid methodologies that provide both PS and DS.

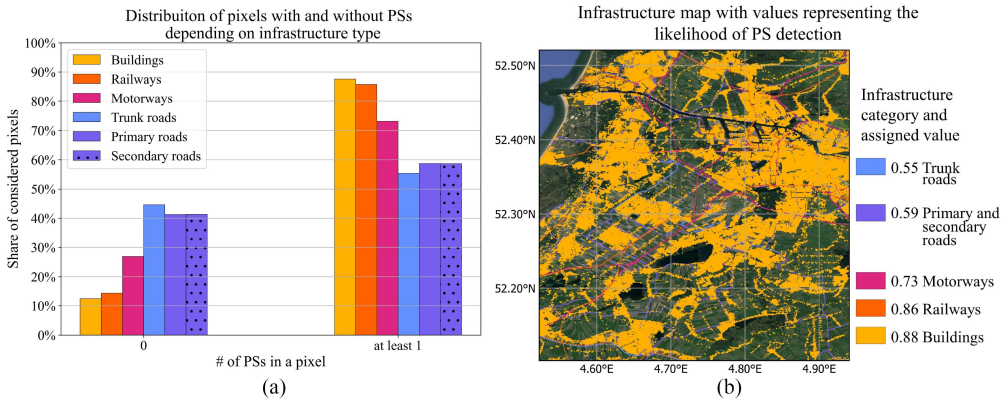

Fig. 3. (a) Distribution of pixels containing a PS over the Netherlands. (b) Snippet of the infrastructure map generated by rasterization of infrastructure location from OSM. The data from subfigure (a) were used in this raster to assign values for specific infrastructure types.

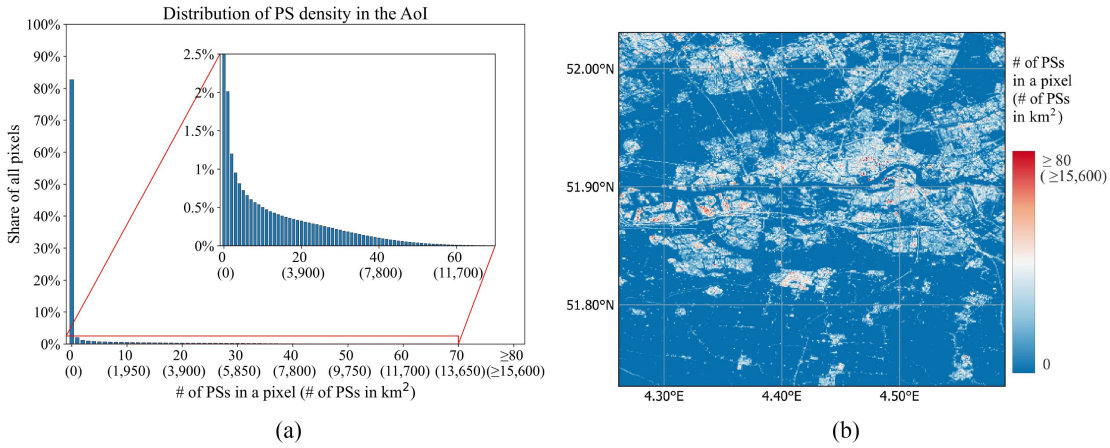

Fig. 4. Distribution of PS density calculated as the number of PSs in a 3-arcsec pixel. (a) PS density distribution in the AoI over the Netherlands. The red rectangle shows a closer look at the plot when the share of pixels is below 2.5%. (b) Map snippet showing an example of the spatial PS distribution in the AoI.

PS density is commonly expressed in PS/km ^{2} units and is used to gauge overall density in a study area or specific land type. This calculation averages over all pixels in the region, each potentially containing a variable number of PS points. A density of 500 PS/km^2, which would translate to just 4 PSs in a pixel given the three arcsec (≈90 m at the equator) resolution of the input raster, is typically considered high coverage [27], particularly in urban studies, where results from Sentinel-1 often exceed this threshold [73], [74]. However, it is crucial to emphasize that not all pixels within a certain area meet this threshold; some may have a higher density, while others might have no PS points at all. To enhance the clarity of the results and because the proposed methodology focused on individual structures rather than comprehensive area monitoring, PS density is reported in this article as the count of PS points within a single pixel. This approach allows users to determine the desired PS point count for successful monitoring of their specific structure of interest. Nevertheless, for readers who might be used to seeing the density of PS expressed in PS/km^2, we added the converted values where appropriate. The size of the pixel changes with latitude, and while three arcsec pixels have a size of roughly 90×90 m^2 at the equator, at 52° N, which is the latitude of Amsterdam, it would be around 57×90 m^2. We assume the latter size of the pixel when converting the pixel-based count of PSs into the density per km^2.

A second input channel was required to ensure a comprehensive representation of roads beyond urban areas. An infrastructure map was generated to guide the model in recognizing spatial patterns between pixels with and without PSs, directing the model's attention to both clustered pixels within cities and those aligned along the linear infrastructure. This involved overlaying PS densities, derived from the EGMS data, onto infrastructure maps based on OSM data that corresponded to selected infrastructure typologies. The process enabled an evaluation of the pixel percentage comprising at least one PS for each infrastructure type considered. These percentages served as values in a combined raster representing all infrastructure types [depicted in Fig. 3(b)]. The highest assigned value was retained when a pixel encompassed multiple OSM elements (e.g., a building and a primary road).

2) Implementation and Training of the ML Model: To achieve the primary objective of this study, the correlation between long-term coherence, infrastructure location data, and the presence of PSs was modeled. The PS density followed a zero-inflated reverse J-shaped distribution, with most pixels lacking PSs, as depicted in Fig. 4(a). Spatial inconsistency

further complicated the dataset with no clear clusters of pixels with a similar PS count visible [see Fig. 4(b)]. Due to the characteristics of data continuity and pixel-to-pixel variations, we adopted a pixelwise regression approach. In this way, we exploited the data variations to facilitate a more precise pixel-level image classification rather than focusing on distinct categories for semantic segmentation labels. A decoder-encoder architecture, namely, the U-Net architecture, was adopted to preserve image resolution.

The U-Net model was implemented with five layers. We employed the ResNet [75] as an encoder to exploit short skip connections between consecutive ResNet modules and long skip connections between respective modules in the U-Net model's encoder and decoder path. This approach yields improved outcomes compared to the VGG16 proposed in the original U-Net approach [76].

Integrating the two input channels and ground truth rasters was crucial to ensure an appropriate dataset for training. First, all inputs were processed to have identical resolutions and be spatially aligned. As long-term coherence data were provided in a tiled format, the dataset was divided into training, validation, and test sets, allocating 70%, 15%, and 15% of each tile to their respective splits (see Fig. 2).

Different strategies were employed for generating data batches during training versus validation and testing. The training dataset split was sampled randomly, facilitating the extraction of patches from spatially diverse regions within one batch. Sampling parameters were configured to ensure coverage across the entire training area with minimal overlap. Random augmentation was applied to increase batch variability and enhance prediction accuracy [77]. This involved horizontal and vertical flips, along with 90° rotations for each input channel and corresponding mask, each implemented with a 50% probability of occurrence.

The corresponding data splits were sampled using a regular grid for validation and testing, guaranteeing comprehensive coverage without overlap. Fig. 2 provides an example of patch locations in one random batch from each split. For the geospatial manipulations of the dataset and the model implementation, the TorchGeo library was used, which is specifically designed for deep learning applications on geospatial data [78].

ML models are characterized by hyperparameters that regulate the models' performance. For some of them, decisions were made based on informed choices, while others were determined through a random grid search from predefined options. Random initial weights were used, as commonly applied pretrained weights, such as ImageNet [79], are trained on entirely different types of input data. We prevented overfitting with an early stopping function that was implemented instead of a search for the best number of epochs. Thus, the training was stopped if the change in validation loss was smaller than 0.01 for more than 15 epochs. A learning rate scheduler was also utilized to decrease the learning rate if validation loss plateaued for at least ten epochs. The identity function served as the activation function, as it is best suited for pixelwise regression tasks [60]. Given the data distribution and that the method aimed to predict both common low and sparse high values of the mask, Mean Absolute Error (MAE) loss was chosen due to its suitability for handling such an imbalanced input. Finally, to determine patch size, batch size, backbone (encoder), learning rate, and parameters of AdamW optimizer, a grid search was conducted considering the options detailed in Table I.

TABLE I
LIST OF MODEL PARAMETERS TUNED WITH RANDOM GRID SEARCH

Hyper-parameter	Range	Final model selection
Batch size	[8, 16, 32]	16
Patch size	[64, 128, 256]	64
Backbone	[resnet18, resnet34, resnet50]	resnet34
Learning rate	Random sampling in different orders of magnitude from range [0.0001, 0.001]	0.00776601
Weight decay	[0.0001, 0.001, 0.01]	0.01
Momentum parameter	[0.9, 0.99, 0.999]	0.9
Squared gradient parameter	[0.9, 0.99, 0.999]	0.99

Once the optimal parameters were selected, the model training was run. Each batch was normalized after each encoder and decoder block when passing through the U-Net architecture, enhancing training speed and performance [80].

IV. RESULTS

A. Seasonal Long-Term Coherence

Histograms in Fig. 5(a), (c), and (e) present the distribution of pixels covering infrastructure in predefined long-term coherence bins for each season. A clear seasonal trend is observed, with similar values for spring, summer, and fall, and a noticeably higher share of pixels in the highest coherence bins in winter. This trend is evident for all infrastructure types considered, with the most pronounced difference observed for roads. Fig. 5(b), (d), and (f) show changes in the NDVI between summer and winter. The NDVI can range from -1 to 1, where values close to 1 indicate dense vegetation, e.g., a rainforest, low values, usually around 0, indicate that there is no vegetation in a pixel, and negative values can be attributed to water. Given the relationship between interferometric coherence and NDVI [81], the seasonal variation can be attributed to lower NDVI in winter (see Fig. 5), indicating smaller vegetation that covers transportation networks and buildings to a lesser extent, allowing for more stable radar reflection with higher long-term coherence.

However, for the ML model training, it was not important to identify the seasonal long-term coherence raster with the highest values but rather the one best suited for infrastructure recognition. Visual comparisons between the two extreme seasons, summer and winter, revealed that despite overall higher coherence in winter, as indicated by the histograms, roads are more observable on the summer long-term coherence map (see in Fig. 10(a) and (b) in the Appendix). To understand the phenomenon, the comparison considered the mean and standard deviation of NDVI for each season. In the region marked as A in Fig. 10(a), an evident seasonal variation in the mean NDVI is observed [see Fig. 10(c) and (d)]. The overall lower winter NDVI

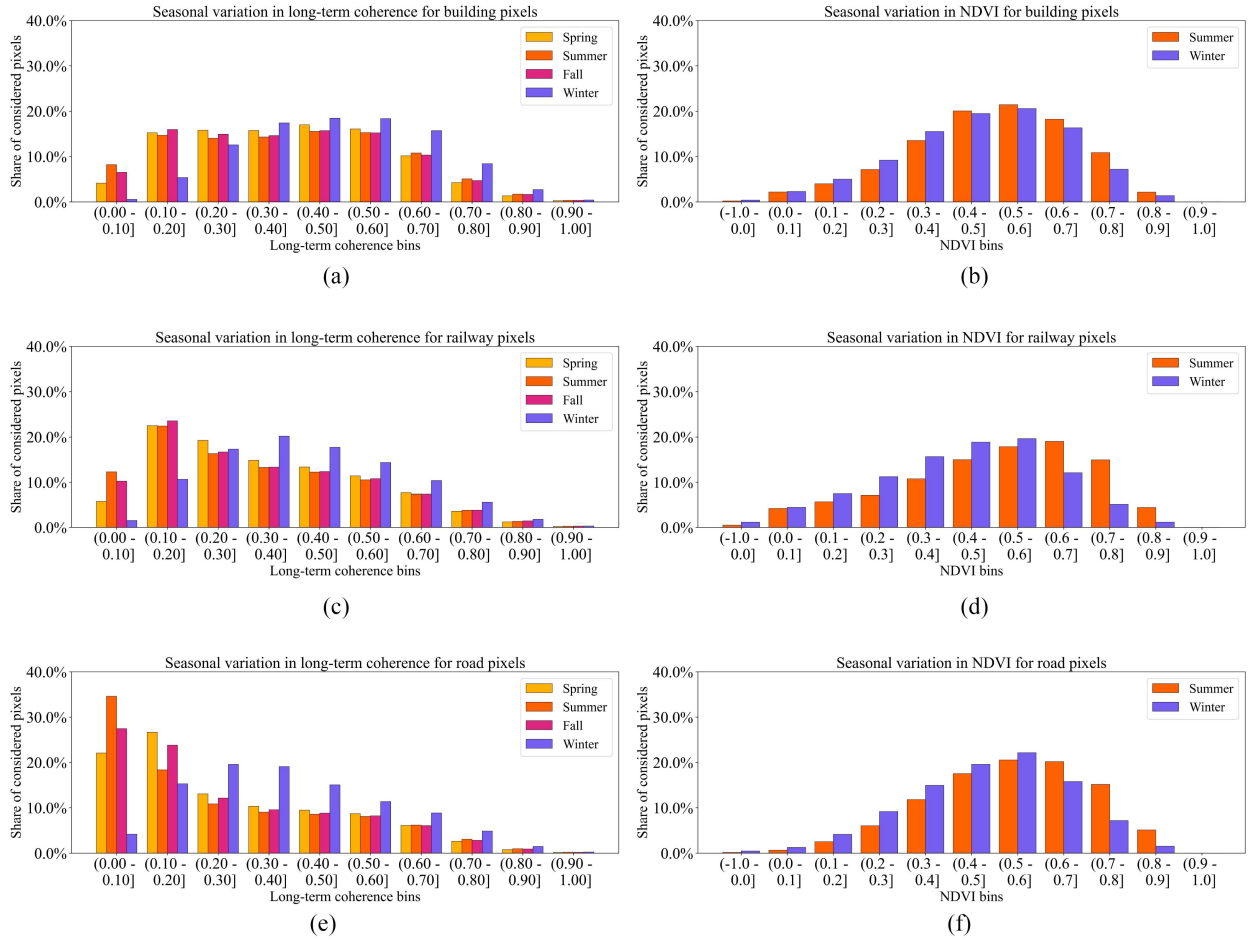

Fig. 5. Seasonal fluctuations in long-term coherence (a), (c), and (e) and NDVI (b), (d), and (f) over the Netherlands. (a) and (b) show data for buildings, (c) and (d) for railways, and (e) and (f) for motorways, trunk, primary, and secondary roads that are collectively treated as road pixels. The size of the pixel is three arcsec.

caused by smaller vegetation and, thus, higher coherence, blends fields with roads, making the latter difficult to distinguish. For the region labeled B in Fig. 10(b), the mean NDVI is comparable and relatively high, possibly due to dense vegetation. However, Fig. 10(e) and (f) show that the standard deviation of NDVI for this region is far greater in summer. The lower variability of NDVI in winter is probably caused by smaller changes in vegetation in this season. This makes obtaining relatively stable radar reflection easier despite the significant vegetation covering those pixels but also makes infrastructure harder to differentiate from fields.

Therefore, despite the potential advantages of employing winter radar data for infrastructure monitoring due to its higher overall long-term coherence, the decision to use summer coherence for model training was made. This choice was deemed more suitable as the features are visually more apparent, particularly in rural regions, thereby potentially enhancing the model's ability to recognize spatial patterns.

B. *Infrastructure Map With Values Representing the Likelihood of PS Detection*

The model's second input channel consisted of an infrastructure map, where values represented the probability of detecting PSs. This map was created by evaluating the proportion of pixels containing at least one PS for each OSM data category, as detailed in Fig. 3(a). The analysis revealed that 88% of building pixels, 86% of railway pixels, 73% of motorway pixels, and 55% of trunk pixels contained some PSs. Notably, both primary and secondary roads exhibited an equal share of pixels with at least one PS, amounting to 59%. These statistical outcomes were subsequently employed as values within the infrastructure map raster, as shown in Fig. 3(b).

C. *Results of the Model Training*

The ML model was iteratively trained 20 times, employing the optimal hyperparameter configuration while varying the seed. The seed is a number used for the initialization of a pseudorandom number generator. Modifying the seed for the model used in this study changes the initial state of model parameters and defines how the AoI is divided into test, validation, and training sets. Change of seed can have an effect on the results similar to using a different ML model architecture or different model hyperparameters [82]. Therefore, seed variation was required to quantify the model variance. The mean MAE of pixel-level PS count prediction for the test set was 1.06 ($\approx$207 PS/km^2),

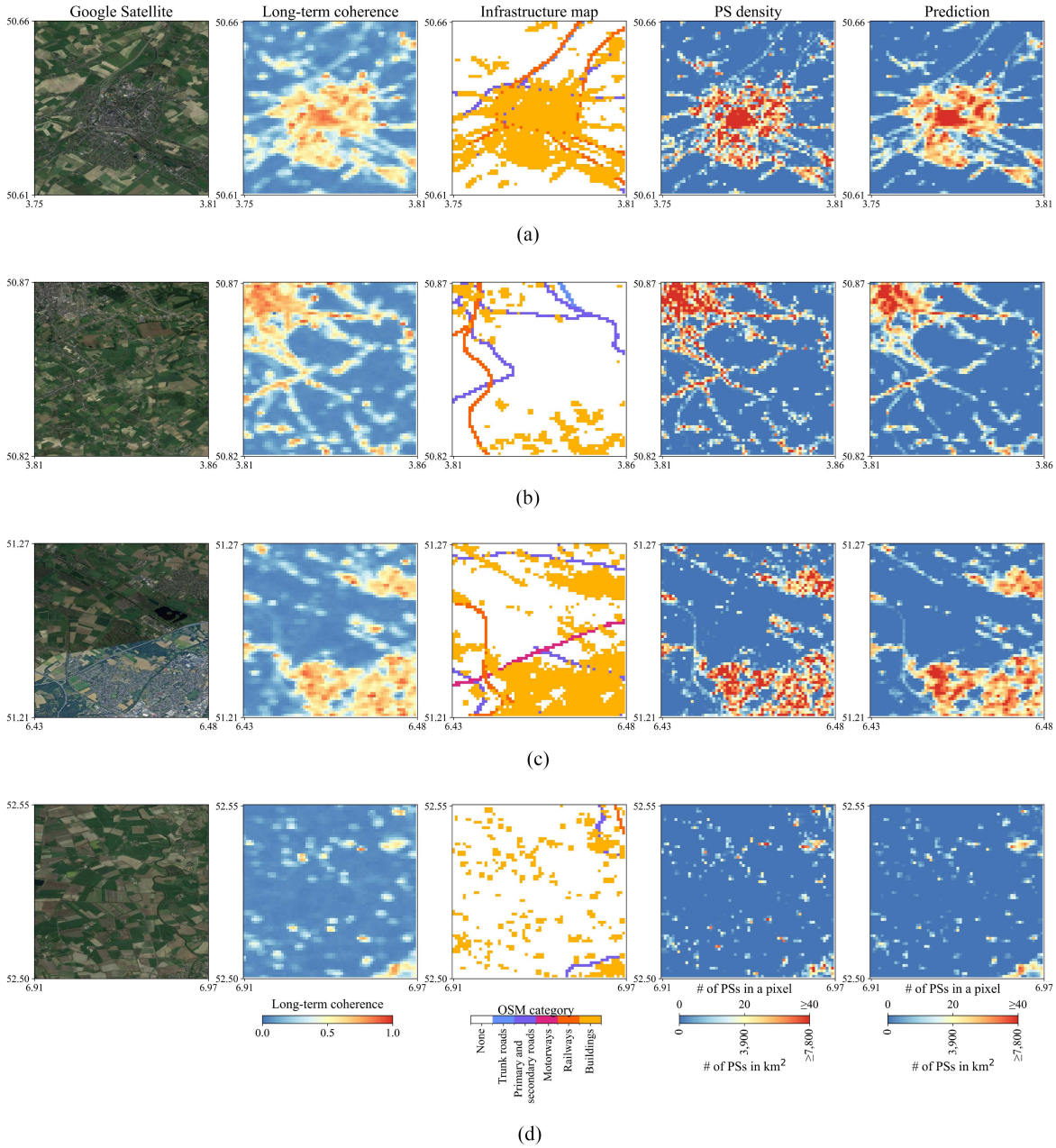

Fig. 6. Example of results on the test split of the AoI covering the Netherlands with columns showing optical satellite imagery from Google, long-term coherence, infrastructure map, PS densities obtained from EGMS, and predicted number of points per pixel. (a) Shows an example of results over an urbanized area, (b) and (c) show predictions for regions with transportation networks, and (d) presents the outcome over rural area with sparsely distributed buildings.

with a standard deviation of 0.10 (≈19 PS/km^2). Discrepancies in results across different seed settings were attributed to variations in the splitting of AoI into training, validation, and test sets and the randomness in sampling into specific batches. In certain instances, the test split encompassed more regions characterized by an overall low density of PSs, such as rural areas or water bodies, resulting in a correspondingly lower overall MAE.

For subsequent result analysis, we specifically selected the test outcomes derived from a seed set to 54 321, which yielded an MAE of 1.19 (≈232 PS/km^2). This selection was motivated by the inclusion of numerous patches containing infrastructure elements in this test split. Given the characteristics of pixelwise regression, the predictions were initially expressed as real numbers. However, considering the pixel-level PSs densities were natural numbers, the model's outcomes were rounded to the nearest integer value.

For visual assessment of model performance, plots were generated comparing 1) inputs, i.e., long-term coherence in summer and OSM-based pixel classification based on road, railway, or building presence, 2) ground-truth mask with a count of PSs in a pixel generated from EGMS data, and 3) predictions from the model. Fig. 6 shows four examples of the results from the test split, demonstrating high accuracy when using the proposed model to predict PS presence on infrastructure assets.

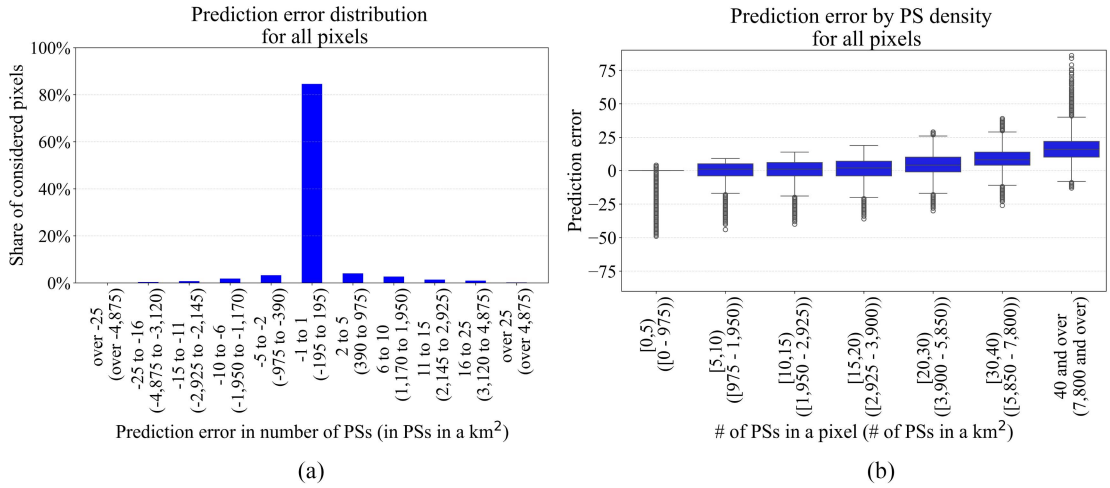

Fig. 7. (a) Histogram and (b) box plot showing the error distribution in the model's test split of the AoI over the Netherlands, considering all pixels. The errors plotted by specific infrastructure type can be found in Appendix A. The prediction error is defined as the difference between the pixel-level PS density generated from EGMS data and the model's prediction. Pixel resolution was three arcsec, which converts to $\approx 57 \times 90$ m^2.

The differences between PS densities obtained from EGMS data (i.e., the ground truth) and model predictions for the test split were analyzed to further evaluate the model's performance. When all pixels from the test split are analyzed, see Fig. 7(a), promising results are achieved, with over 80% of all of the pixels having a predicted value within ± 1 ($\approx$195 PS/km^2) from the actual value. This is because the data are zero-inflated, and the model is remarkably accurate for pixels with less than 5 points ($\approx$975 PS/km^2), as shown on the box plot in Fig. 7(b). Outliers for this bin of PS density suggest that, for low-density pixels, the model sometimes wrongly overestimates. However, the model's accuracy decreases with the increase of PS density. Still, considering the error relative to the actual number of PSs in a pixel, it is acceptable, given that the methodology is intended to be used as a tool for preliminary availability assessment of MT-InSAR results.

The general trend of an increase in the mean value of error with the increase of PS density holds when only pixels belonging to a specific infrastructure category are considered, as shown in the Appendix [see Fig. 11(b), (d), (f), (h), (j), and (l)]. The error for buildings and railways follows a Gaussian distribution [see Fig. 11(a) and (c)], with a similar share of pixels being over- and underestimated. However, for all four types of roads analyzed [see Fig. 11(e), (g), (i), and (k)], the model tends to underestimate the specific PS density. This is especially true for motorways. Still, for over 40% of motorway pixels and over half of the pixels covering the trunk, primary, and secondary roads, the PS density is estimated within 1 PS from the actual value.

D. Assessment of the Model's Generalization

To assess the model's generalization, we applied it to previously unseen data covering a region around Rome, Italy. As shown in Fig. 8, the selected location encompassed multiple transportation networks and a highly urbanized region of Rome, thus making it a suitable test area to prove the model's

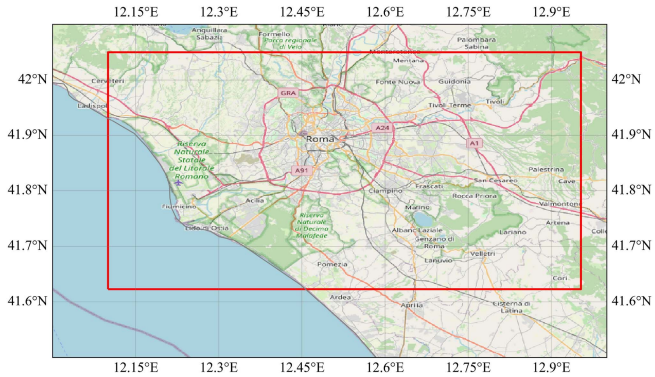

Fig. 8. AoI considered for the assessment generalization, including the city of Rome, Italy.

accuracy over the infrastructure types selected for this study. The model exhibited strong generalization performance, achieving the MAE of 3.61 ± 0.06 ($\approx 704 \pm 12$ PS/km^2). The error is higher than the one obtained from the test split, but this is an expected behavior of the model. The AoI selected for this generalization trial is more urbanized than the AoI over the Netherlands used for model training, validation, and testing shown in Fig. 2. Therefore, as Fig. 9 shows, pixels are more populated with PSs, and thus, the error is higher. However, the error relative to the actual values is acceptable, as confirmed by the visual comparison between input and prediction for this dataset in Fig. 12 in the Appendix. Although some underestimation is noticeable, the model accurately predicted PS density for pixels covering a linear infrastructure and demonstrated high accuracy in predicting pixels without measurement points.

V. Discussion

The results show that the method successfully models the correlation between long-term coherence and PS density. The

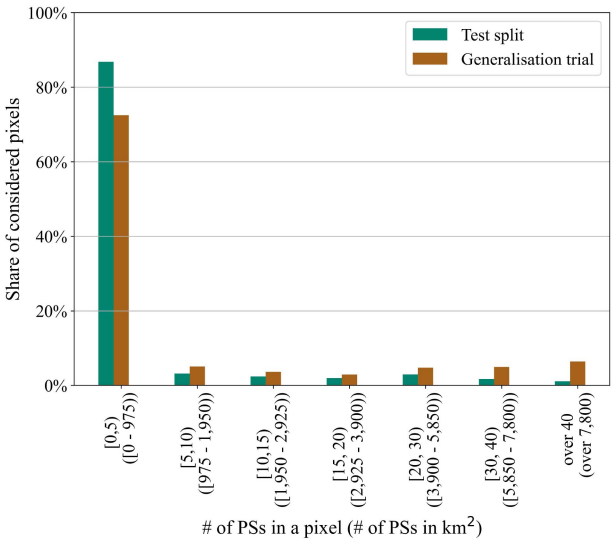

Fig. 9. Comparison of EGMS-based pixel-level PS density distribution between the test split of the AoI over the Netherlands and the generalization trial AoI over Rome, Italy.

proposed workflow provides accurate estimates of the availability of PSs over infrastructure and proves good generalization performance, filling the existing gap in the rapid availability assessment of MT-InSAR outcomes.

The method's ability to predict PS density on a pixel-based level provides an enhancement to previously known methodologies, predominantly reliant on land cover maps characterized by coarser resolution. The increased resolution improves the accuracy of predictions over urban areas and transportation networks, and this advantage is particularly evident in nonurban regions, where the utilization of the infrastructure map as a second input to the model allows for the prediction of PS availability over linear infrastructure. The model was trained with the same settings, but only the coherence as input and outcomes demonstrate notable improvements when the infrastructure map is included, as illustrated in Fig. 13 in the Appendix. In scenarios such as the one depicted, employing a land classification methodology would lead to an underestimation of PS availability on roads, as the area might be misclassified as rural. Moreover, the approach to infrastructure map generation introduces a degree of flexibility to the workflow, enabling users to select and adjust the set of infrastructure typologies according to their specific needs.

The script for generating predictions requires coordinates describing the region of interest and a locally downloaded OSM file covering the AoI. The process involves downloading the appropriate long-term coherence raster, processing the OSM file to create the infrastructure map, reading the trained model, and generating a prediction raster. The execution time varies based on the extent of the AOI, the size of the OSM file, and the hardware used. For example, a test conducted on a laptop (Intel Core i7-6820HK CPU, 32GB RAM, NVIDIA GeForce GTX 1070 GPU with 8GB dedicated vRAM) downloaded the OSM file for the Silesia region in Poland within a minute and generated a prediction for an area of approximately 1320 km^2 in about 5 min. Specifically, the steps were: 1) processing the OSM file to generate the infrastructure map, which took over 4.5 min, 2) downloading the coherence raster, which took 15 s, and 3) generating the prediction raster, which took about 2 s. It is evident that the primary bottleneck is the infrastructure map generation. However, the proposed approach remains faster than downloading and coregistering SAR scenes, especially for regional, national, or global studies. Furthermore, the code is easily scalable, and when run on a high-performance computing system, it can process multiple regions in parallel and generate global-scale predictions within a few days.

Applying the model effectively across different regions requires some additional consideration. The model was trained and tested on European data, with the summer long-term coherence raster selected as the most appropriate for training. There might be pixel-level seasonal changes in coherence due to significant vegetation coverage changing across seasons or snow cover in winter. However, such situations are not expected to occur for the major roads, railways, and buildings examined in this study. Therefore, the coherence of infrastructure is expected to remain consistent between seasons. The selection of specific seasonal coherence was motivated by identifying the season exhibiting the most distinct differences between infrastructure and surrounding pixels, aiding the model in learning. Tests with other seasonal coherence maps and different combinations of them confirmed that they did not enhance the model's predictions. However, if the method is applied to other regions, especially in the southern hemisphere, reconsidering this choice and opting for the winter long-term coherence might be necessary. Further testing is recommended for Northern America, where long-term coherence rasters in [49] are prepared using ascending, not descending, geometry acquisitions.

The accuracy of the model prediction depends on the accuracy of the inputs. While the OSM database used to generate the infrastructure map is frequently updated, the coherence map was created from data acquired in 2019–2020. New constructions in previously rural, low-coherence areas could alter the pixel-level coherence significantly in such a case. Thus, an updated coherence map should be considered as input to the model. However, if new infrastructure has been constructed in an urbanized area, the model is expected to accurately predict the PS availability, provided it is supplied with an infrastructure map generated from updated OSM data.

As illustrated in Fig. 14(a) in the Appendix, the model occasionally produced blurred predictions, especially in urban regions where pixels with very high densities (depicted in red on the plot) were often underestimated. Addressing this could involve: 1) enlarging the input dataset to provide more examples of pixels with high densities during training, 2) handling data imbalance through resampling or synthetic data creation, 3) using the long-term coherence raster with a higher resolution to reduce spatial averaging, or 4) fine-tuning hyperparameters to find combination enhancing predictions in regions densely populated with PSs.

While OSM is a valuable data source, its completeness and quality vary spatially, and inaccuracies within it may lead the model to mistakenly assume the absence of infrastructure in a

pixel. Moreover, the model was fed only with information about buildings, railways, and some types of roads, as those were the infrastructure types of interest for this study. In Fig. 14(b) in the Appendix, an example shows how PSs were not predicted over an airport because those pixels were set to zero on the infrastructure map used as the second input to the model. Therefore, to improve predictions, it might be beneficial to include information about additional infrastructure types, such as airports or industrial buildings, in the second input channel raster. Alternatively, exploring other data sources, such as optical data, could help the model learn PS locations independently of assumptions made during OSM-based infrastructure map generation. However, as shown in the Appendix in Fig. 14(c), when the coherence is relatively high, the model provides accurate predictions even when the infrastructure map does not identify any assets due to the OSM incompleteness. These correct predictions are possible thanks to the U-Net's ability to identify spatial patterns.

Instances of overestimation occurred when pixels with relatively high coherence were predicted to contain PSs, even though the ground truth mask showed otherwise. As seen in the Appendix in Fig. 15(a), this behavior might be explained by the displacement affecting this particular part of the road as shown in the Appendix in Fig. 15(c). The long-term coherence remained high due to the spatial averaging included in the calculation of the interferometric coherence, even when no PSs were present in that pixel. In addition, the linear deformation assumption in the EGMS data may cause discrepancies when pixels are affected by nonlinear deformations, such as seasonal displacement [42].

Finally, model discrepancies could also stem from an underestimation of PS density, where low long-term coherence leads to no PS prediction, but a few measurement points are present in the ground truth mask, as shown in the Appendix in Fig. 15(b). This model behavior may also occur when movement affects the considered area (see Fig. 15(d) in the Appendix), resulting in a loss of spatially averaged interferometric coherence. However, some pixels might still serve as effective radar targets and qualify as PS, even though they are surrounded by poor-quality pixels, emphasizing the advantage of using MT-InSAR over a standard InSAR.

It should also be highlighted that while the model estimated the number of PSs in a pixel that included infrastructure, it could not accurately predict the exact location of measurement points. Thus, even in a densely populated pixel, there is no guarantee of a PS being located on the structure in question. Nevertheless, a higher PS density in a particular pixel increases the likelihood of some PSs covering the structure. Although having information about the movement of a specific point on a structure is valuable for evaluating its structural condition, a higher density of PS points allows for a more accurate estimation of the deformation pattern. This, in turn, enhances the understanding of potential failure mechanisms affecting structural health. Hence, a structure with a higher density of PS can be monitored better. Performing a statistical analysis of the relationship between PS density per pixel and the actual number of measurement points on structures could help set thresholds, guiding stakeholders in understanding the applicability of MT-InSAR for monitoring specific structures. Moreover, the exact number of PSs found on the investigated structure will depend on the data and the specific algorithm used for the analysis. Nevertheless, it should be acknowledged that the model exhibited exceptional performance in accurately predicting pixels without PSs, providing a way to easily identify assets that are unsuitable for MT-InSAR monitoring and require an alternative way of monitoring.

VI. Conclusion

This article introduces an innovative approach for an initial assessment of the suitability of MT-InSAR for the monitoring of buildings and transportation networks. The objective was achieved by developing a ML model able to capture the correlation between long-term coherence and PS density. Using the U-Net neural network architecture for pixelwise regression, we established a robust relationship between the long-term coherence parameter of the coherence decay model, pixel-level infrastructure presence data, and information about PS availability. The proposed workflow provides a way for predicting PS density, addressing the current lack of an early predictor for MT-InSAR outcome availability without the need for time-intensive data analysis.

We chose to employ summer long-term coherence as model input. The analysis revealed that the infrastructure is easier to differentiate from other pixels on plots in the summer, facilitating enhanced visual recognition despite the overall higher long-term coherence in winter. We showed the impact of the mean and standard deviation of NDVI in summer and winter on the long-term coherence. To guide the model in accurately identifying spatial patterns, we generated an infrastructure map including buildings, railways, and roads (motorway, trunk, primary, and secondary, specifically), assigning values corresponding to the likelihood of PS detection to each of the selected infrastructure types. The proposed methodology exhibits adaptability, permitting customization of the infrastructure map to suit the specific requirements of users who may seek emphasis on particular infrastructure typologies. The model achieved the MAE of 1.06 ± 0.10 ($\approx 207 \pm 19$ PS/km^2) in pixel-based PS count on the test split, and the visual assessment of model predictions confirmed its high accuracy. Notably, the technique demonstrated remarkable reliability in predicting pixels without PS, a consequence of the zero-inflated nature of the input data. While occasional underestimations occurred in high-density pixels, the error relative to the actual count of PSs was deemed acceptable. The robust generalization performance proved the model's applicability across diverse spatial regions.

MT-InSAR does not guarantee uniform measurement points coverage, and the challenge of forecasting outcomes' availability remains a bottleneck in applying this technique as a complementary SHM technique. The proposed approach fills the gap and surpasses previous methodologies reliant on land cover classifications, offering more precise results with an increased spatial resolution, thereby assisting radar data experts and infrastructure assets stakeholders in determining the feasibility of monitoring a specific asset with Sentinel-1 data. Consequently, this capability enhances the usability of spaceborne remote sensing in SHM, informing stakeholders' decision-making process and contributing to advancements in developing sustainable and resilient infrastructure.

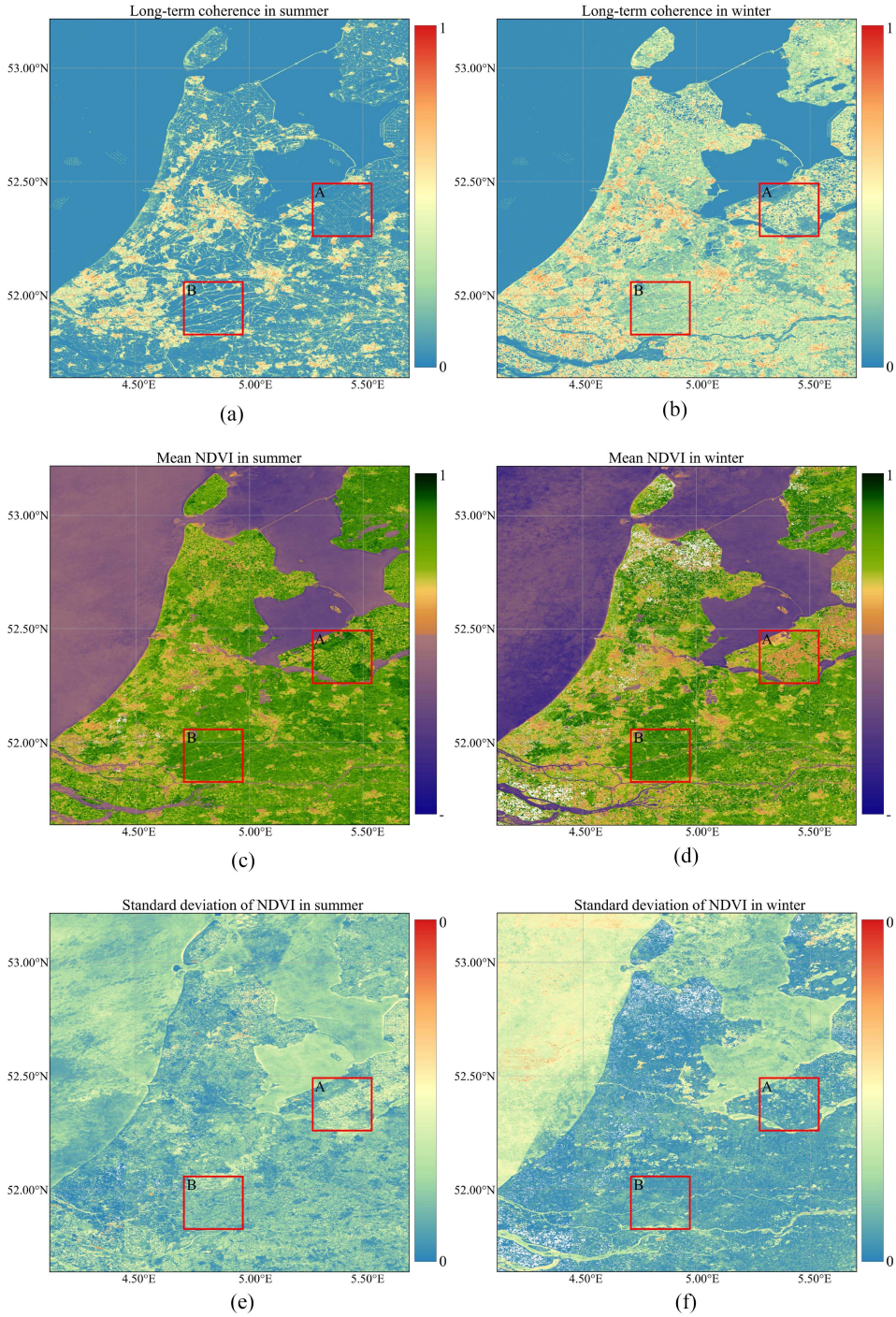

Fig. 10. Long-term coherence and NDVI parameters for summer and winter in the Amsterdam area. A comparison between (a) summer and (b) winter long-term coherence highlights the seasonal differences in the coherence. The seasonal mean of NDVI is shown in (c) for summer and (d) for winter, followed by the variation in the seasonal standard deviation of NDVI as presented in (e) for summer and (f) for winter. Some pixels on subplots (c)–(f) appear white, indicating a lack of NDVI data due to the area being consistently covered by clouds throughout the entire period under consideration.

APPENDIX
ADDITIONAL FIGURES

The appendix contains additional figures that support the results. Fig. 10 presents visual differences between summer and winter long-term coherence and NDVI characteristics. Fig. 11 extends Fig. 7 by showing the prediction errors for specific infrastructure types. The following figures illustrate model performance on previously unseen data (see Fig. 12), with and without infrastructure map used as input (see Fig. 13), and on some specific examples of under- and overestimation (see Figs. 14 and 15).

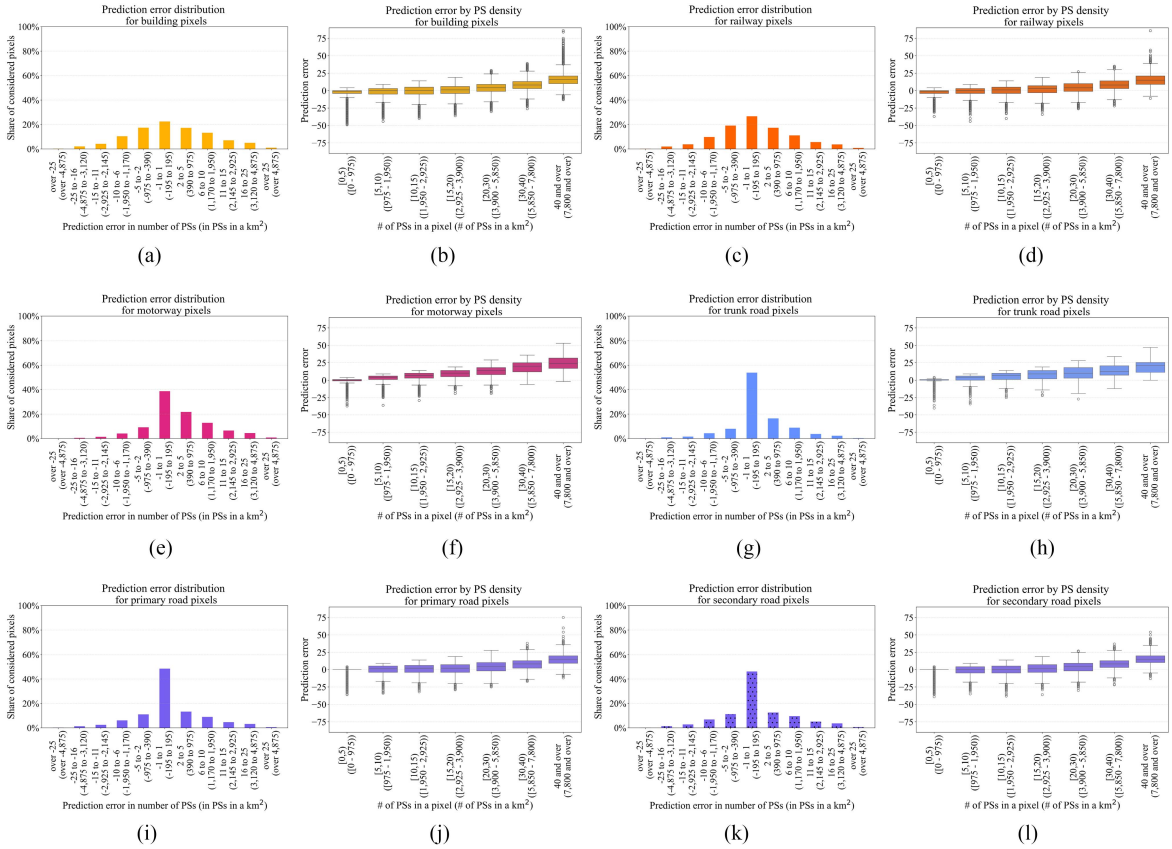

Fig. 11. Histograms and box plots depicting the error distribution in the model's test split of the AoI over the Netherlands, considering specific infrastructure types separately, i.e., (a) and (b) buildings, (c) and (d) railways, (e) and (f) motorways, (g) and (h) trunk roads, (i) and (j) primary roads, and (k) and (l) secondary roads. The prediction error is defined as the difference between the pixel-level PS density generated from EGMS data and the model's prediction. Pixel resolution was three arcsec, which converts to $\approx 57 \times 90 \mathrm{m}^2$.

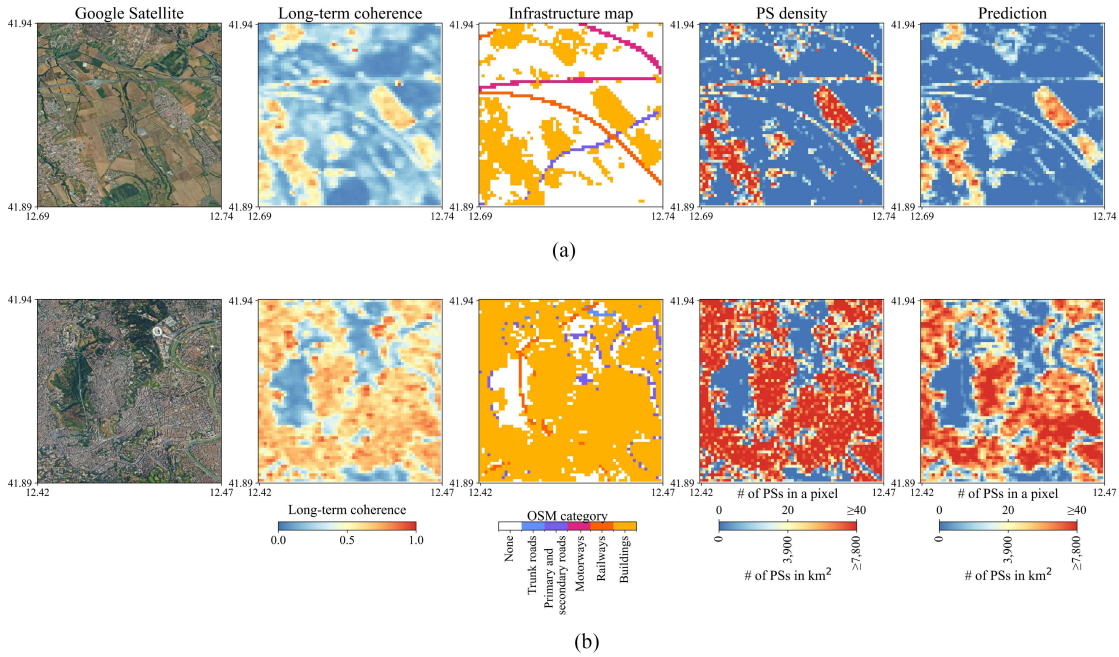

Fig. 12. Visualization of model inputs and prediction performance on data previously unseen by the model in the vicinity of Rome, Italy. Examples show the model's performance over: (a) a region with multiple roads and a railway, and (b) a highly urbanized area.

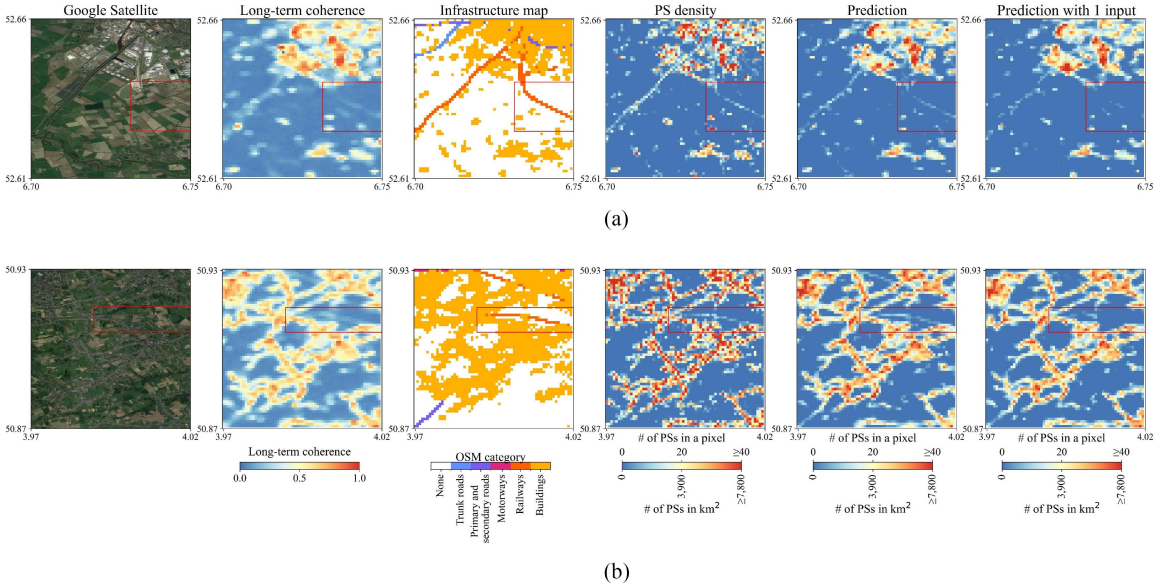

Fig. 13. Visualization of model input and prediction performance employing one (sixth column) and two (fifth column) input channels. The two examples show how the addition of the infrastructure map to the model improved the PS density predictions over an infrastructure asset in (a) rural area and (b) relatively close to the urban environment.

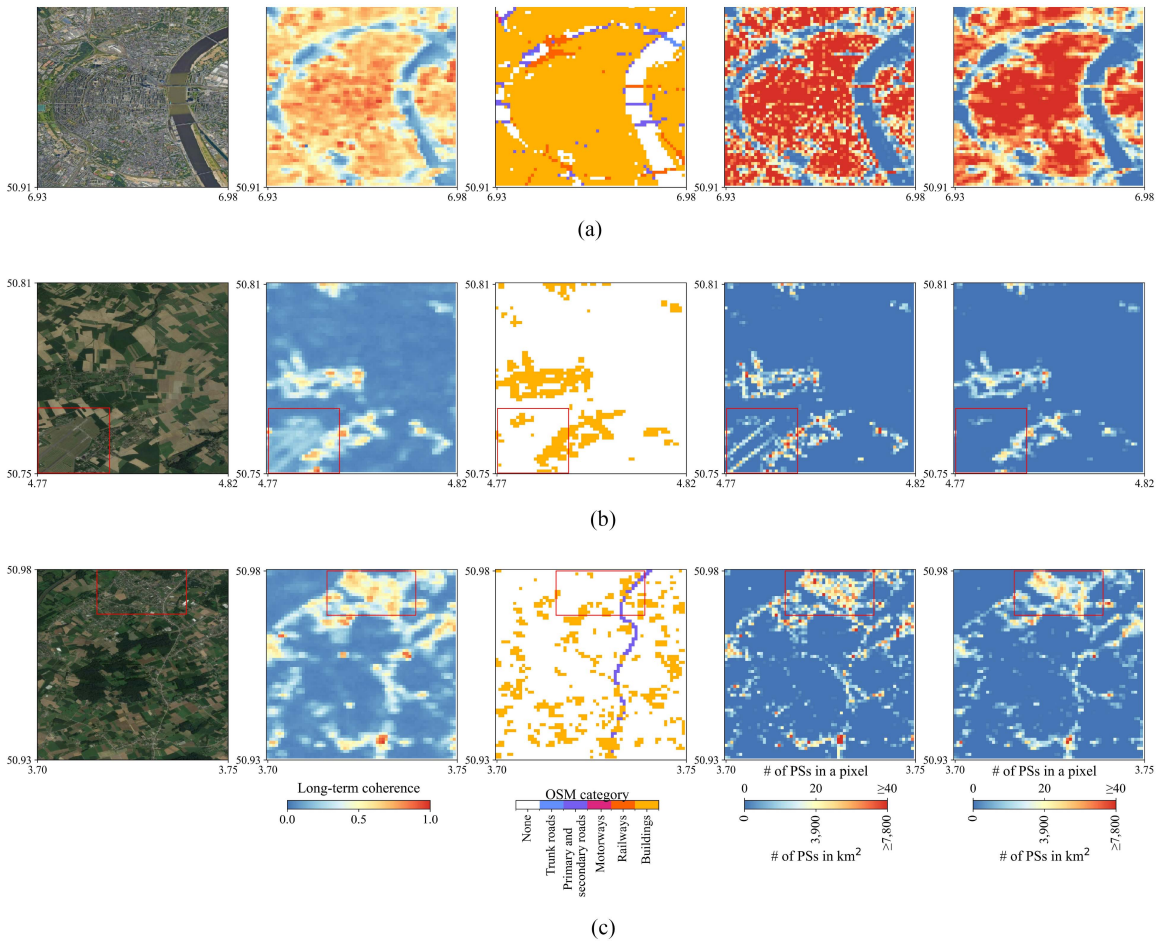

Fig. 14. Visualization of model performance specifically highlighting: (a) underestimations in urban regions, (b) underestimation attributed to the method employed for infrastructure map generation, and (c) accurate predictions of PS density even though the infrastructure map is not correctly identifying the infrastructure.

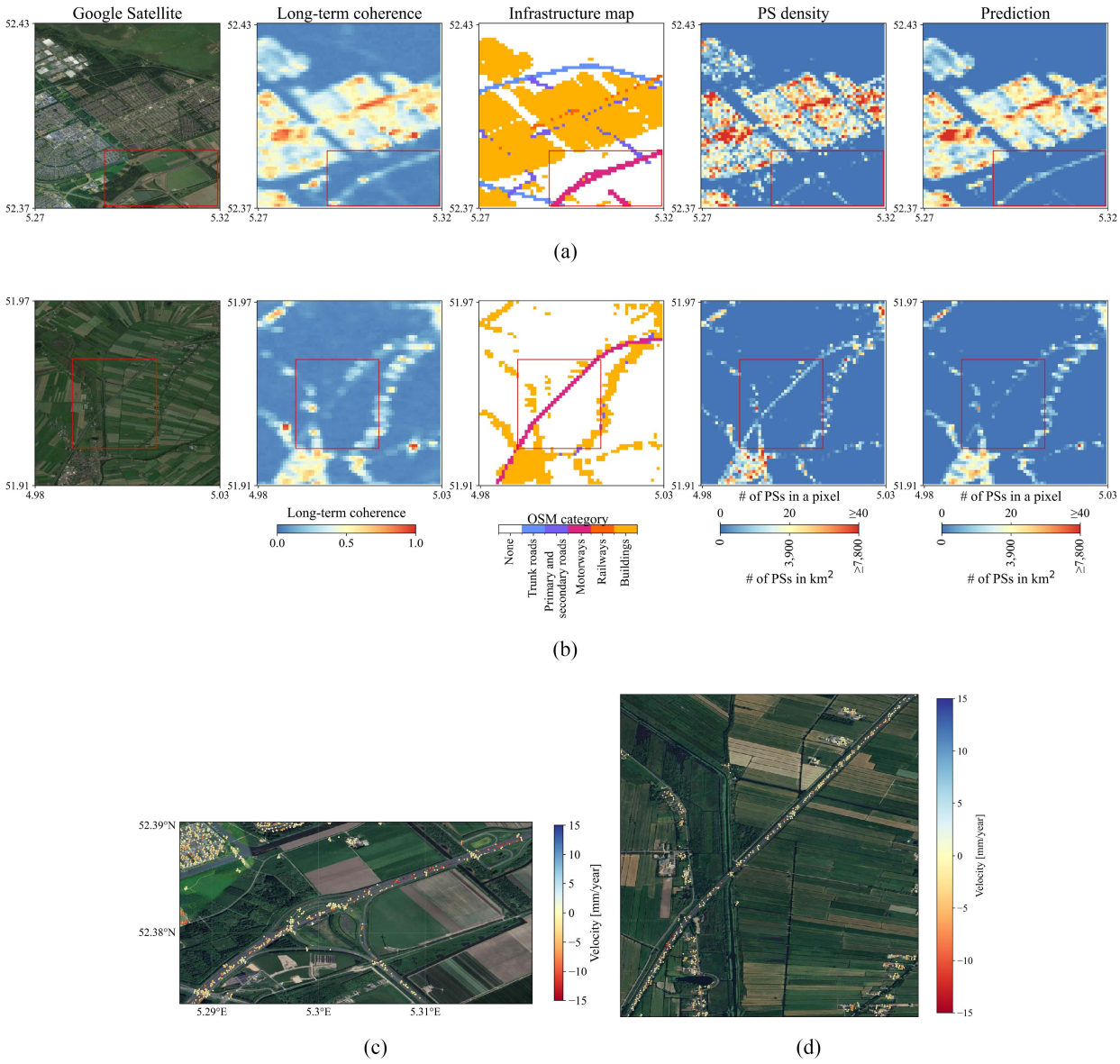

Fig. 15. Visualization of model performance specifically highlighting (a) overestimation in the prediction and (b) underestimation in the prediction. Both overestimation and underestimation stem from deformation patterns evident in PS maps generated from EGMS results, as shown in (c) covering the area outlined by the red box in (a), and (d) the region from the red box in (b).

ACKNOWLEDGMENT

The authors would like to thank Dr. Alice Cicirello for the valuable discussion and her insights on the ML approach.

REFERENCES

[1] J.-P. Rodrigue and T. Notteboom, "Transportation and economic development," in *The Geography of Transport Systems*, 3rd Ed. Evanston, IL, USA: Routledge, 2013, pp. 226–236.

[2] K. C. Sinha, S. Labi, and B. R. D. K. Agbelie, "Transportation infrastructure asset management in the new millennium: Continuing issues, and emerging challenges and opportunities," *Transportmetrica A: Transport Sci.*, vol. 13, no. 7, pp. 591–606, 2017.

[3] B. T. Adey, "A road infrastructure asset management process: Gains in efficiency and effectiveness," *Infrastructure Asset Manage.*, vol. 6, no. 1, pp. 2–14, 2019.

[4] A. K. Agrawal, G. Washer, S. Alampalli, X. Gong, and R. Cao, "Evaluation of the consistency of bridge inspection quality in New York State," *J. Civil Struct. Health Monit.*, vol. 11, no. 5, pp. 1393–1413, 2021.

[5] B. A. Graybeal, B. M. Phares, D. D. Rolander, M. Moore, and G. Washer, "Visual inspection of highway bridges," *J. Nondestruct. Eval.*, vol. 21, no. 3, pp. 67–83, 2002.

[6] J. Cao and X. Liu, *Wireless Sensor Networks for Structural Health Monitoring, Ser. SpringerBriefs in Electrical and Computer Engineering*. Berlin, Germany: Springer, 2016.

[7] A. Leventis and K. Papadopoulos, "Wireless sensor networks: Routing protocol for critical infrastructure protection," in *Trusted Computing for Embedded Systems*, B. Candaele, D. Soudris, and I. Anagnostopoulos, Eds. Berlin, Germany: Springer, 2015, pp. 227–246.

[8] S. Laflamme et al., "Roadmap on measurement technologies for next generation structural health monitoring systems," *Meas. Sci. Technol.*, vol. 34, no. 9, 2023, Art. no. 093001.

[9] S. Sony, S. Laventure, and A. Sadhu, "A literature review of next-generation smart sensing technology in structural health monitoring," *Struct. Control Health Monit.*, vol. 26, no. 3, 2019, Art. no. e2321.

[10] J. J. Sousa et al., "Potential of multi-temporal InSAR techniques for bridges and dams monitoring," *Procedia Technol.*, vol. 16, pp. 834–841, 2014.

[11] J. C. Curlander and R. N. McDonough, *Synthetic Aperture Radar: Systems and Signal Processing, Ser. Wiley Series in Remote Sensing*. Hoboken, NJ, USA: Wiley, 1991.

[12] R. Bamler and P. Hartl, "Synthetic aperture radar interferometry," *Inverse Problems*, vol. 14, no. 4, 1998, Art. no. R1.

[13] P. Rosen et al., "Synthetic aperture radar interferometry," *Proc. IEEE*, vol. 88, no. 3, pp. 333–382, Mar. 2000.

[14] D. Massonnet et al., "The displacement field of the landers earthquake mapped by radar interferometry," *Nature*, vol. 364, no. 6433, pp. 138–142, 1993.

[15] J. Biggs and T. J. Wright, "How satellite InSAR has grown from opportunistic science to routine monitoring over the last decade," *Nature Commun.*, vol. 11, no. 1, 2020, Art. no. 3863.

[16] H. Zebker and J. Villasenor, "Decorrelation in interferometric radar echoes," *IEEE Trans. Geosci. Remote Sens.*, vol. 30, no. 5, pp. 950–959, Sep. 1992.

[17] R. F. Hanssen, "Radar interferometry: Data interpretation and error analysis," Ph.D. dissertation, Civil Eng. Geosci., Delft Univ. Technol., Delft, The Netherlands, 2001.

[18] A. Ferretti, C. Prati, and F. Rocca, "Permanent scatterers in SAR interferometry," *IEEE Trans. Geosci. Remote Sens.*, vol. 39, no. 1, pp. 8–20, Jan. 2001.

[19] A. Ferretti, C. Prati, and F. Rocca, "Nonlinear subsidence rate estimation using permanent scatterers in differential SAR interferometry," *IEEE Trans. Geosci. Remote Sens.*, vol. 38, no. 5, pp. 2202–2212, Sep. 2000.

[20] V. Macchiarulo, P. Milillo, C. Blenkinsopp, C. Reale, and G. Giardina, "Multi-temporal InSAR for transport infrastructure monitoring: Recent trends and challenges," *Proc. Inst. Civil Eng.: Bridge Eng.*, vol. 176, no. 2, pp. 92–117, 2023.

[21] P. Milillo, G. Giardina, D. Perissin, G. Milillo, A. Coletta, and C. Terranova, "Pre-collapse space geodetic observations of critical infrastructure: The Morandi Bridge, Genoa, Italy," *Remote Sens.*, vol. 11, no. 12, 2019, Art. no. 1403.

[22] G. Giardina, P. Milillo, M. J. DeJong, D. Perissin, and G. Milillo, "Evaluation of InSAR monitoring data for post-tunnelling settlement damage assessment," *Struct. Control Health Monit.*, vol. 26, no. 2, 2019, Art. no. e2285.

[23] A. Ferretti et al., "Submillimeter accuracy of InSAR time series: Experimental validation," *IEEE Trans. Geosci. Remote Sens.*, vol. 45, no. 5, pp. 1142–1153, May 2007.

[24] A. Rucci, A. Ferretti, A. M. Guarnieri, and F. Rocca, "Sentinel 1 SAR interferometry applications: The outlook for sub millimeter measurements," *Remote Sens. Environ.*, vol. 120, pp. 156–163, 2012.

[25] M. Crosetto, O. Monserrat, M. C.-González, N. Devanthéry, and B. Crippa, "Persistent scatterer interferometry: A review," *ISPRS J. Photogrammetry Remote Sens.*, vol. 115, pp. 78–89, 2016.

[26] S. Plank, J. Singer, and K. Thuro, "Assessment of number and distribution of persistent scatterers prior to radar acquisition using open access land cover and topographical data," *ISPRS J. Photogrammetry Remote Sens.*, vol. 85, pp. 132–147, 2013.

[27] V. Macchiarulo, P. Milillo, C. Blenkinsopp, and G. Giardina, "Monitoring deformations of infrastructure networks: A fully automated GIS integration and analysis of InSAR time-series," *Struct. Health Monit.*, vol. 21, no. 4, pp. 1849–1878, 2022.

[28] C. Clementini, D. Latini, V. Gagliardi, L. B. Ciampoli, F. D'Amico, and F. D. Frate, "Synergistic monitoring of transport infrastructures by multitemporal InSAR and GPR technologies: A case study in Salerno, Italy," in *Proc. SPIE Conf. Earth Resour., Environ. Remote Sens./GIS Appl. XII*, 2021, pp. 148–157.

[29] A. L. V. Natijne, T. A. Bogaard, F. J. V. Leijen, R. F. Hanssen, and R. C. Lindenbergh, "World-wide InSAR sensitivity index for landslide deformation tracking," *Int. J. Appl. Earth Observ. Geoinf. Citation*, vol. 111, 2022, Art. no. 102829.

[30] S. Plank, J. Singer, C. Minet, and K. Thuro, "Pre-survey suitability evaluation of the differential synthetic aperture radar interferometry method for landslide monitoring," *Int. J. Remote Sens.*, vol. 33, no. 20, pp. 6623–6637, 2012.

[31] D. Notti, J. C. Davalillo, G. Herrera, and O. Mora, "Assessment of the performance of X-band satellite radar data for landslide mapping and monitoring: Upper Tena Valley case study," *Natural Hazards Earth Syst. Sci.*, vol. 10, no. 9, pp. 1865–1875, 2010.

[32] D. Notti, C. Meisina, F. Zucca, and A. Colombo, "Models to predict persistent scatterers data distribution and their capacity to register movement along the slope," in *Proc. Fringe 2011 Workshop*, 2011 pp. 17–23.

[33] D. Notti, G. Herrera, S. Bianchini, C. Meisina, J. C. G.-Davalillo, and F. Zucca, "A methodology for improving landslide PSI data analysis," *Int. J. Remote Sens.*, vol. 35, no. 6, pp. 2186–2214, 2014.

[34] F. Cigna, L. B. Bateson, C. J. Jordan, and C. Dashwood, "Simulating SAR geometric distortions and predicting persistent scatterer densities for ERS-1/2 and ENVISAT C-band SAR and InSAR applications: Nationwide feasibility assessment to monitor the landmass of Great Britain with SAR imagery," *Remote Sens. Environ.*, vol. 152, pp. 441–466, 2014.

[35] G. Bru et al., "Suitability assessment of X-band satellite SAR data for geotechnical monitoring of site scale slow moving landslides," *Remote Sens.*, vol. 10, no. 6, 2018, Art. no. 936.

[36] M. D. Soldato, L. Solari, A. Novellino, O. Monserrat, and F. Raspini, "A new set of tools for the generation of InSAR visibility maps over wide areas," *Geosciences*, vol. 11, no. 6, 2021, Art. no. 229.

[37] S. Auer, S. Hinz, and R. Bamler, "Ray-tracing simulation techniques for understanding high-resolution SAR images," *IEEE Trans. Geosci. Remote Sens.*, vol. 48, no. 3, pp. 1445–1456, Mar. 2010.

[38] A. Ferretti, A.M. Guarnieri, C. Prati, F. Rocca, and D. Massonnet, *InSAR Principles: Guidelines for SAR Interferometry Processing and Interpretation*, vol. TM-19. Noordwijk, The Netherlands: ESA Pub., 2007.

[39] F. Meyer, "Spaceborne synthetic aperture radar: Principles, data access, and basic processing techniques," in *The SAR Handbook: Comprehensive Methodologies for Forest Monitoring and Biomass Estimation*, A. Flores, K. Herndon, R. Thapa, and E. Cherrington, Eds. Washington, DC, USA: NASA, 2019, pp. 20–63.

[40] G. Franceschetti, A. Iodice, and D. Riccio, "A canonical problem in electromagnetic backscattering from buildings," *IEEE Trans. Geosci. Remote Sens.*, vol. 40, no. 8, pp. 1787–1801, Aug. 2002.

[41] D. Perissin and A. Ferretti, "Urban-target recognition by means of repeated spaceborne SAR images," *IEEE Trans. Geosci. Remote Sens.*, vol. 45, no. 12, pp. 4043–4058, Dec. 2007.

[42] M. Crosetto et al., "The evolution of wide-area DInSAR: From regional and national services to the European ground motion service," *Remote Sens.*, vol. 12, no. 12, pp. 1–20, 2020.

[43] L. Chang, R. P. B. J. Dollevoet, and R. F. Hanssen, "Monitoring line-infrastructure with multisensor SAR interferometry: Products and performance assessment metrics," *IEEE J. Sel. Topics Appl. Earth Observ. Remote Sens.*, vol. 11, no. 5, pp. 1593–1605, May 2018.

[44] N. Fiorentini, M. Maboudi, P. Leandri, M. Losa, and M. Gerke, "Surface motion prediction and mapping for road infrastructures management by PS-InSAR measurements and machine learning algorithms," *Remote Sens.*, vol. 12, no. 23, 2020, Art. no. 3976.

[45] N. Fiorentini, M. Maboudi, M. Losa, and M. Gerke, "Assessing resilience of infrastructures towards exogenous events by using PS-InSAR-based surface motion estimates and machine learning regression techniques," *ISPRS Ann. Photogrammetry, Remote Sens. Spatial Inf. Sci.*, vol. 5, pp. 19–26, 2020.

[46] H. Zebker and K. Chen, "Accurate estimation of correlation in InSAR observations," *IEEE Geosci. Remote Sens. Lett.*, vol. 2, no. 2, pp. 124–127, Apr. 2005.

[47] F. Sica, A. Pulella, M. Nannini, M. Pinheiro, and P. Rizzoli, "Repeat-pass SAR interferometry for land cover classification: A methodology using Sentinel-1 short-time-series," *Remote Sens. Environ.*, vol. 232, 2019, Art. no. 111277.

[48] A. Parizzi, X. Y. Cong, and M. Eineder, "First results from multifrequency interferometry. a comparison of different decorrelation time constants at L, C and X band," in *ESA Special Pub.*, H. Lacoste, Ed., vol. 677. 2010, Art. no. 5.

[49] J. Kellndorfer et al., "Global seasonal Sentinel-1 interferometric coherence and backscatter data set," *Sci. Data*, vol. 9, no. 1, pp. 1–16, 2022.

[50] Y. LeCun, Y. Bengio, and G. Hinton, "Deep learning," *Nature*, vol. 521, no. 7553, pp. 436–444, 2015.

[51] E. Shelhamer, J. Long, and T. Darrell, "Fully convolutional networks for semantic segmentation," *IEEE Trans. Pattern Anal. Mach. Intell.*, vol. 39, no. 4, pp. 640–651, Apr. 2017.

[52] O. Ronneberger, P. Fischer, and T. Brox, "U-Net: Convolutional networks for biomedical image segmentation," in *Proc. Int. Conf. Med. Image Comput. Comput.-Assist. Interv.*, N. Navab, J. Hornegger, W. M. Wells, and A. F. Frangi, Eds. Berlin, Germany, 2015, pp. 234–241.

[53] J. V. Solórzano, J. F. Mas, Y. Gao, and J. A. G.-Cruz, "Land use land cover classification with U-Net: Advantages of combining Sentinel-1 and Sentinel-2 imagery," *Remote Sens.*, vol. 13, no. 18, 2021, Art. no. 3600.

[54] P. Shamsolmoali, M. Zareapoor, R. Wang, H. Zhou, and J. Yang, "A novel deep structure U-Net for sea-land segmentation in remote sensing images," *IEEE J. Sel. Topics Appl. Earth Observ. Remote Sens.*, vol. 12, no. 9, pp. 3219–3232, Sep. 2019.
[55] B. Grabowski, M. Ziaja, M. Kawulok, and J. Nalepa, "Towards robust cloud detection in satellite images using U-Nets," in *2021 IEEE Int. Geosci. Remote Sens. Symp.*, 2021, pp. 4099–4102.
[56] Z. Zhang, Q. Liu, and Y. Wang, "Road extraction by deep residual U-Net," *IEEE Geosci. Remote Sens. Lett.*, vol. 15, no. 5, pp. 749–753, May 2018.
[57] Z. Chen, C. Wang, J. Li, N. Xie, Y. Han, and J. Du, "Reconstruction bias U-Net for road extraction from optical remote sensing images," *IEEE J. Sel. Topics Appl. Earth Observ. Remote Sens.*, vol. 14, pp. 2284–2294, 2021.
[58] H. Wang and F. Miao, "Building extraction from remote sensing images using deep residual U-Net," *Eur. J. Remote Sens.*, vol. 55, no. 1, pp. 71–85, 2022.
[59] C. Wu et al., "Building damage detection using U-Net with attention mechanism from pre- and post-disaster remote sensing datasets," *Remote Sens.*, vol. 13, no. 5, 2021, Art. no. 905.
[60] W. Yao, Z. Zeng, C. Lian, and H. Tang, "Pixel-wise regression using U-Net and its application on pansharpening," *Neurocomputing*, vol. 312, pp. 364–371, 2018.
[61] K. Radhakrishnan, K. A. Scott, and D. A. Clausi, "Sea ice concentration estimation: Using passive microwave and SAR data with a U-Net and curriculum learning," *IEEE J. Sel. Topics Appl. Earth Observ. Remote Sens.*, vol. 14, pp. 5339–5351, 2021.
[62] M. A. Najar, G. Thoumyre, E. W. J. Bergsma, R. Almar, R. Benshila, and D. G. Wilson, "Satellite derived bathymetry using deep learning," *Mach. Learn.*, vol. 112, no. 4, pp. 1107–1130, 2023.
[63] T. N. Carlson and D. A. Ripley, "On the relation between NDVI, fractional vegetation cover, and leaf area index," *Remote Sens. Environ.*, vol. 62, no. 3, pp. 241–252, 1997.
[64] N. Pettorelli, J. O. Vik, A. Mysterud, J.-M. Gaillard, C. J. Tucker, and N. C. Stenseth, "Using the satellite-derived NDVI to assess ecological responses to environmental change," *Trends Ecol. Evol.*, vol. 20, no. 9, pp. 503–510, 2005.
[65] A. Veloso et al., "Understanding the temporal behavior of crops using Sentinel-1 and Sentinel-2-like data for agricultural applications," *Remote Sens. Environ.*, vol. 199, pp. 415–426, 2017.
[66] M. Haklay, "How good is volunteered geographical information? A comparative study of OpenStreetMap and ordnance survey datasets," *Environ. Plan. B: Plan. Des.*, vol. 37, no. 4, pp. 682–703, 2010.
[67] C. B.-Leigh and A. M.-Ball, "The world's user-generated road map is more than 80% complete," *PLoS One*, vol. 12, no. 8, 2017, Art. no. e0180698.
[68] B. Herfort, S. Lautenbach, J. P. d. Albuquerque, J. Anderson, and A. Zipf, "A spatio-temporal analysis investigating completeness and inequalities of global urban building data in OpenStreetMap," *Nature Commun.*, vol. 14, no. 1, 2023, Art. no. 3985.
[69] M. Minaei, "Evolution, density and completeness of OpenStreetMap road networks in developing countries: The case of Iran," *Appl. Geogr.*, vol. 119, 2020, Art. no.102246.
[70] Q. Zhou and H. Lin, "Investigating the completeness and omission roads of OpenStreetMap data in Hubei, China by comparing with street map and street view," *Int. Arch. Photogrammetry, Remote Sens. Spatial Inf. Sci.*, vol. XLIII-B4-2020, pp. 299–306, 2020.
[71] Y. Larsen et al., "European ground motion service: Service implementation plan and product specification document," Copernicus Land Monitoring Service, 2020. Accessed: Sep. 12, 2023. [Online]. Available: https://land.copernicus.eu/en/products/european-ground-motion-service
[72] A. Ferretti and E. Passera, "Algorithm theoretical basis document," 2023. Accessed: Sep. 13, 2023. [Online]. Available: https://eospso.nasa.gov/content/algorithm-theoretical-basis-documents
[73] R. Bonì, A. Bosino, C. Meisina, A. Novellino, L. Bateson, and H. McCormack, "A methodology to detect and characterize uplift phenomena in urban areas using Sentinel-1 data," *Remote Sens.*, vol. 10, no. 4, 2018, Art. no. 607.
[74] J. Wasowski, F. Bovenga, R. Nutricato, D. O. Nitti, and M. T. Chiaradia, "Detection and monitoring of slow landslides using Sentinel-1 multi-temporal interferometry products," in *Advancing Culture of Living With Landslides*, M. Mikos, B. Tiwari, Y. Yin, and K. Sassa, Eds. Berlin, Germany: Springer, 2017, pp. 249–256.
[75] K. He, X. Zhang, S. Ren, and J. Sun, "Deep residual learning for image recognition," in *2016 IEEE Conf. Comput. Vis. Pattern Recognit.*, 2016, pp. 770–778.
[76] N. Siddique, S. Paheding, C. P. Elkin, and V. Devabhaktuni, "U-Net and its variants for medical image segmentation: A review of theory and applications," *IEEE Access*, vol. 9, pp. 82 031–82 057, 2021.
[77] X. Hao, L. Liu, R. Yang, L. Yin, L. Zhang, and X. Li, "A review of data augmentation methods of remote sensing image target recognition," *Remote Sens.*, vol. 15, no. 3, 2023, Art. no. 827.
[78] A. J. Stewart, C. Robinson, I. A. Corley, A. Ortiz, J. M. L. Ferres, and A. Banerjee, "TorchGeo: Deep learning with geospatial data," in *Proc. 30th Int. Conf. Adv. Geographic Inf. Syst.*, 2022, pp. 1–12.
[79] J. Deng, W. Dong, R. Socher, L.-J. Li, K. Li, and L. F.-Fei, "ImageNet: A large-scale hierarchical image database," in *Proc. 2009 IEEE Conf. Comput. Vis. Pattern Recognit.*, 2009, pp. 248–255.
[80] S. Ioffe and C. Szegedy, "Batch normalization: Accelerating deep network training by reducing internal covariate shift," in *Proc. 32nd Int. Conf. Mach. Learn.*, 2015, pp. 448–456.
[81] Y. Chen, Q. Sun, and J. Hu, "Quantitatively estimating of InSAR decorrelation based on landsat-derived NDVI," *Remote Sens.*, vol. 13, no. 13, 2021, Art. no. 2440.
[82] J. Mehrer, C. J. Spoerer, N. Kriegeskorte, and T. C. Kietzmann, "Individual differences among deep neural network models," *Nature Commun.*, vol. 11, no. 1, 2020, Art. no. 5725.

Dominika Malinowska received the M.Sc. degree in astronautics and space engineering from Cranfield University, Cranfield, U.K. She is currently working toward the Ph.D. degree (with a thesis on the space-borne assessment of infrastructure conditions) with the University of Bath, Bath, U.K., and is a Guest Student with the Delft University of Technology, Delft, The Netherlands.

Her research interests include the use of MT-InSAR to assess the structural vulnerability of infrastructure assets on a national and global scale, focusing on data availability and multihazard risk-based assessment.

Ms. Malinowska was the recipient of the Course Director's prize for excellent overall performance with the Cranfield University.

Pietro Milillo (Senior Member, IEEE) received the bachelor's degree (Laurea) and the master's degree in physics, with a thesis on synthetic aperture radar and GPS data processing, from the University of Bari, Bari, Italy, in 2012, and the Ph.D. degree in environmental engineering, with a thesis on the synergistic use of synthetic aperture radar (SAR) constellations for studying natural and anthropogenic phenomena, from the University of Basilicata, Potenza, Italy, in 2016.

Over the years, he has held various positions, including NASA Postdoctoral Program (NPP) Fellow with JPL, Scientist in radar science and engineering with JPL, and Associate Project Scientist in Earth system science with the University of California, Irvine, CA, USA. Since 2021, he has been an Assistant Professor in geosensing system engineering with the Department of Civil and Environmental Engineering, University of Houston, Houston, TX, USA. He is also a Guest Scientist with the German Aerospace Center (DLR), Munich, Germany. He has authored or coauthored more than thirty-two research articles in leading international journals. His research focuses on the synergistic use of remote sensing data exploitation and innovative approaches for computational analyses in Earth and cryosphere science and natural/anthropogenic hazard response. He is particularly interested in analyzing how the new generation of remote sensing instruments leads to a more effective, near real-time disaster monitoring, assessment, and response. His multidisciplinary research interests [funded by NASA, DLR, and the Italian Space Agency (ASI)] include Earth science, cryosphere, and disaster response.

Kevin Briggs received the bachelor's degree in civil engineering from the University of Bath, Bath, U.K., in 2006, and an Engineering Doctorate (EngD) degree from the University of Southampton, Southampton, U.K., in 2011.

He is currently an Associate Professor of Geomechanics and RAEng/HS2 Ltd Senior Research Fellow of Geotechnical Engineering with the University of Southampton. His research interests include geotechnical engineering, engineering geology and hydrogeology involve instrumentation, and field monitoring and its interpretation. This has been used to assess the condition of infrastructure earthworks and their deterioration in response to ageing, extreme weather and a changing climate.

He is a Member of the International Society for Soil Mechanics and Geotechnical Engineering (ISSMGE) Technical Committee for Transportation Geotechnics (TC202) and a Member of the UK Department for Transport (DfT) College of Experts.

Cormac Reale received the B.E. degree (first class hons) in civil and environmental engineering from University College Cork, Ireland, in 2011 and the Ph.D. degree in geotechnical engineering from University College Dublin, Ireland, in 2015.

He is currently a Geotechnical Lecturer with the Department of Architecture and Civil Engineering, the University of Bath, Bath, U.K. His research interest focuses on structural health monitoring, and his work primarily revolves around analyzing aged slope networks and offshore foundations, aiming to develop optimized design, maintenance, and remediation strategies. Within this domain he utilizes a mixture of field work, laboratory testing, and probabilistic analysis to quantify infrastructure resilience and determine areas of critical concern.

Giorgia Giardina received the M.S. degree (summa cum laude) in environmental engineering from the University of Brescia, Brescia, Italy, in 2007, and the Ph.D. degree in civil engineering from the Delft University of Technology, Delft, The Netherlands, in 2013.

She was an Assistant Professor with the University of Bath, U.K., a Visiting Professor with the NASA Jet Propulsion Laboratory, USA, and a Research Associate with the University of Cambridge, U.K. She is currently an Associate Professor in geo-monitoring and data analytics with the Delft University of Technology and the "Sensing from Space" Theme Leader with the Delft Space Institute. Her research interests include remote sensing and computational modeling, multihazard risk and damage assessment, heritage protection, and infrastructure resilience.

Dr. Giardina is a Member of the Earthquake Engineering Field Investigation Team (EEFIT) management committee, the International Scientific Committee on the Analysis and Restoration of Structures of Architectural Heritage (ISCARSAH), the Centre for Global Heritage and Development (CGHD), and the 4TU Centre for Resilience Engineering (4TU RE).